



HAL
open science

Ray-Tracing Analysis for the Propagation of Saturn Narrowband Emission Within the Saturnian Magnetosphere

Siyuan Wu, Ulrich Taubenschuss, Shengyi Ye, Georg Fischer, Baptiste Cecconi, Mengmeng Wang, Tao Tao, Minyi Long, Peng Lu, Yuqi Liu, et al.

► **To cite this version:**

Siyuan Wu, Ulrich Taubenschuss, Shengyi Ye, Georg Fischer, Baptiste Cecconi, et al.. Ray-Tracing Analysis for the Propagation of Saturn Narrowband Emission Within the Saturnian Magnetosphere. Journal of Geophysical Research: Planets, 2024, 129, 10.1029/2023JE008118 . insu-04853455

HAL Id: insu-04853455

<https://insu.hal.science/insu-04853455v1>

Submitted on 23 Dec 2024

HAL is a multi-disciplinary open access archive for the deposit and dissemination of scientific research documents, whether they are published or not. The documents may come from teaching and research institutions in France or abroad, or from public or private research centers.

L'archive ouverte pluridisciplinaire **HAL**, est destinée au dépôt et à la diffusion de documents scientifiques de niveau recherche, publiés ou non, émanant des établissements d'enseignement et de recherche français ou étrangers, des laboratoires publics ou privés.

Copyright

Special Section:

The Frontiers in Jupiter Science and Exploration

Key Points:

- A 3D ray-tracing analysis is conducted for Saturn Narrowband (NB) emissions
- The L-O mode NB emissions propagate toward high latitudes and the Z mode NB emissions are trapped near Saturn
- Small electron density structures on the plasma torus can lead to trapping and depolarization of NB emissions

Correspondence to:

S. Ye,
yesy@sustech.edu.cn














Citation:

Wu, S., Taubenschuss, U., Ye, S., Fischer, G., Cecconi, B., Wang, M., et al. (2024). Ray-tracing analysis for the propagation of Saturn narrowband emission within the Saturnian magnetosphere. *Journal of Geophysical Research: Planets*, 129, e2023JE008118. <https://doi.org/10.1029/2023JE008118>

Received 27 SEP 2023

Accepted 19 MAR 2024

Ray-Tracing Analysis for the Propagation of Saturn Narrowband Emission Within the Saturnian Magnetosphere

Siyuan Wu^{1,2} , Ulrich Taubenschuss³ , Shengyi Ye¹ , Georg Fischer⁴ , Baptiste Cecconi² , Mengmeng Wang¹ , Tao Tao¹ , Minyi Long⁵ , Peng Lu⁵, Yuqi Liu¹ , William S. Kurth⁶ , Caitriona M. Jackman⁷ , Philippe Zarka² , Claire Baskevitch², and Xuedong Feng¹ 

¹Department of Earth and Space Sciences, Southern University of Science and Technology, Shenzhen, People's Republic of China, ²LESIA, Observatoire de Paris, Université PSL, CNRS, Sorbonne Université, Université de Paris Meudon, Paris, France, ³Department of Space Physics, Institute of Atmospheric Physics of the Czech Academy of Sciences, Prague, Czech Republic, ⁴Independent Researcher, Graz, Austria, ⁵Department of Space Physics, School of Electronic Information, Wuhan University, Wuhan, People's Republic of China, ⁶Department of Physics and Astronomy, University of Iowa, Iowa City, IA, USA, ⁷School of Cosmic Physics, DIAS Dunsink Observatory, Dublin Institute for Advanced Studies, Dublin, Ireland

Abstract This study investigates the propagation characteristics of Saturn's Narrowband (NB) emissions using a 3D ray-tracing code incorporating Saturn's magnetic field and electron density parameters. The potential source regions and propagation zones of the L-O mode, Z mode and whistler mode NB emissions are distinguished. The L-O mode NB emissions, generated along local electron plasma frequency surfaces through mode conversion, exhibit straight-line propagation but undergo reflections between the ionosphere, the plasma torus, and the magnetosheath. The slot region, characterized by a lower electron density distributed around the plasma torus boundary, significantly influences emission propagation, potentially leading to trapping and depolarization. The 5 kHz Z mode NB emissions propagate and fill the trapping region delineated by lower cut-off and upper hybrid resonance frequencies. In contrast, the 20 kHz Z mode NB emissions are primarily confined near source regions at the north and south edges of the plasma torus, with the possibility of escaping under variable plasma conditions.

Plain Language Summary Scientists have discovered low-frequency radio waves near Saturn, roughly at 5 and 20 kHz, using data from the Voyager and Cassini spacecrafts. These waves are referred to as narrowband (NB) emissions. The NB emissions are thought to originate from Saturn, but exhibit a puzzling propagation pattern when they propagate far away from their source region. Recent studies propose that the 5 kHz waves might be bouncing off a dense plasma area in Saturn's magnetosheath, introducing intriguing yet not fully understood propagation characteristics. This study employs a numerical approach, that is, the ray-tracing technique, to trace the likely paths of these waves. Drawing on earlier theoretical studies, we pinpoint the potential origins of these waves. Our results indicate that most of these waves, particularly the so-called L-O mode emissions, tend to travel toward Saturn's high latitudes. This directional preference is due to interference from a dense plasma torus in Saturn's equatorial region. The boundary of this torus can trap these waves. Meanwhile, the so-called Z mode waves are confined to a specific region near Saturn. Our study unveils intricate features such as multiple reflections and refractions of these waves near Saturn, shedding light on various data observations.

1. Introduction

Saturn narrowband (NB) emissions were discovered during the Voyager 1 Saturn fly-by (Gurnett et al., 1981). They usually appear as Z- or L-O mode emissions with the wave frequency bands near both 5 and 20 kHz (Menietti et al., 2015, 2018a; Wang et al., 2010; Wu et al., 2021; Ye et al., 2009, 2010a). Whistler mode NB emissions are also observed in the 5 kHz frequency band but have not been studied in detail (Menietti, Averkamp, Ye, Sulaiman, et al., 2018). The generation of L-O mode NB emissions is attributed to a mode conversion mechanism from Z mode waves (Menietti et al., 2016, 2019; Ye et al., 2009), while the Z mode NB emissions are likely produced by the presence of unstable plasma near Saturn (Menietti et al., 2016, 2019), or mode converted from the enhanced electrostatic upper hybrid waves (Ye et al., 2009). Direction-finding analysis indicates that the source regions of 5 kHz Z mode NB emissions are located either in the high latitude auroral region near Saturn's Kilometric Radiation (SKR) source or in the equatorial region near the inner edge of the dense plasma torus

(Lamy et al., 2009; Menietti, Averkamp, Ye, Sulaiman, et al., 2018), formed by the cryovolcanic activities of the Saturn's icy moon Enceladus - a significant source of plasma for the inner magnetosphere (Persoon et al., 2006, 2020). Recent investigations (Kinrade et al., 2023; Wing et al., 2020) have explored the relation between energetic neutral atoms and NB emissions. These findings indicate a probable connection between the generation mechanism of NB emissions, particularly in the 5 kHz band, and events known as type-2 injections (Mitchell et al., 2015). These injections transport hot plasma to the inner magnetosphere in proximity to the plasma torus and are proposed to be a source of temperature anisotropy for the generation of the NB emissions. The injected hot plasma also provides favorable conditions for the excitation of the lower hybrid waves and whistler mode chorus emissions, which may further erode the temperature anisotropy (Wing et al., 2020). Notably, the NB emissions usually show modulation features (Wang et al., 2010; Wu, Ye, et al., 2023; Ye et al., 2016), which exhibit a good correlation to the periodic plasma injections (Kinrade et al., 2023; Wing et al., 2020). Hence, the source regions and the free energy of the wave generation for the NB emissions may also be tied to these hot plasma injection events.

The observations of NB emissions indicate various propagation characteristics that still require theoretical explanations. For instance, the L-O mode NB emissions, originally generated by mode conversion from the Z mode waves near a density gradient interior to the plasma torus, are expected to propagate freely but are probably reflected by the dense plasma torus in the equatorial region, ultimately propagating toward high latitudes. Wu et al. (2022) suggested that the 5 kHz L-O mode NB emissions may undergo reflection at the magnetosheath and be redirected back to the equatorial region outside the plasma torus, while the 20 kHz L-O mode NB emissions can escape from the magnetosphere, creating an equatorial shadow zone (Wu et al., 2021, 2022).

The Z mode NB emissions are trapped in a region close to Saturn, restricted by the lower cut-off frequency ($f_z = \frac{1}{2}(\sqrt{f_{ce}^2 + 4f_{pe}^2} - f_{ce})$, f_{ce} is the electron cyclotron frequency, and f_{pe} is the electron plasma frequency) and the upper hybrid resonance frequency ($f_{uh} = \sqrt{f_{ce}^2 + f_{pe}^2}$). Specifically, the resonance frequency of Z mode waves indeed relies on the wave normal angle (WNA, the angle between the ambient magnetic field and the wave vector), which is known as the Z mode infinity or the upper oblique resonance ($f_i = \frac{1}{\sqrt{2}}[f_{uh}^2 + (f_{uh}^4 - 4f_{ce}^2 f_{pe}^2 \cos^2(\theta))^{1/2}]^{1/2}$, where θ represents the WNA; Beghin et al., 1989; Benson et al., 2006). Generally, f_i is smaller than f_{uh} , matching f_{uh} only when the WNA is 90°. When the WNA is close to zero, f_i can closely match either the local f_{pe} or f_{ce} , whichever is higher. As a result, Z mode waves may be in resonance at different positions when propagating with varying WNA. The trapping region (TR) of Z mode (between f_z and f_i) can be further divided into two regions. In TR-1, where the wave frequency (f_{wave}) is larger than the local f_{pe} , and where the Z mode exhibits right-hand circular polarization (Z_{R-X} mode, slow Z mode); and TR-2, where f_{wave} is smaller than the local f_{pe} , where the Z mode shows left-hand circular polarization (Z_{L-X} mode, fast Z mode). The detailed propagation of these Z mode waves within the trapping regions is still unknown. The presence of dual modulation periods in NB emissions observed within a single hemisphere (Wu, Ye, et al., 2023; Ye, Gurnett, et al., 2010), as opposed to the modulation of SKR which shows one period per hemisphere (Fischer et al., 2015; Gurnett et al., 2009; Lamy, 2011; Ye et al., 2016), implies that Z mode NB emissions in the TR may traverse to the opposite hemisphere before mode converting to L-O mode.

This study aims to investigate the propagation characteristics of NB emissions in both 5 and 20 kHz bands, encompassing both Z- and L-O mode NB emissions. The propagation zone of whistler mode NB emissions is also determined. The ray-tracing method and the adapted Saturn's plasma environments are detailed in Section 2. Section 3 presents and discusses a typical observation of the 5 and 20 kHz NB emissions. In Section 4, we discuss the potential source regions of Saturn NB emissions based on previous theories. The simulation results of L-O and Z mode NB emissions are presented in Sections 5–7. Finally, we discuss and summarize the results in Section 8.

2. Data and Methodology

This study utilizes the Artemis-P (Anisotropic Ray Tracer for Electromagnetics in Magnetosphere, Ionosphere, and Solar Wind, including Polarization) 3-D ray-tracing code (Gautier, 2013; Gautier et al., 2013; Gautier et al., 2023) to calculate radio wave ray paths in a magnetized plasma environment. The code is based on the Haselgrove equations (Haselgrove, 1963; Haselgrove & Haselgrove, 1960):

$$\frac{dx_i}{dt} = J * u_i - K * Y v_i, \quad (1)$$

$$\frac{du_i}{dt} = L * \frac{\partial X}{\partial x_i} + \sum_{j=1}^3 (K * u_j + M * Y v_j) \frac{\partial Y_j}{\partial x_i}, \quad (2)$$

For $i = 1, 2, 3$ specifies the x, y, z components of \mathbf{u} , where

$$J = 2(2(1 - X - Y^2)p + Y(1 + (\mathbf{v} \cdot \mathbf{u})^2)), \quad (3)$$

$$K = -2X(\mathbf{v} \cdot \mathbf{u})(pY - 1), \quad (4)$$

$$L = Y(1 - Y^2)p^2 - 2(1 - X - Y^2)p - Y, \quad (5)$$

$$M = 2Xp(pY - 1), \quad (6)$$

with $X = \frac{f_{pe}^2}{f^2}$ and $Y = \frac{k_z}{f}$. The variable \mathbf{u} is a vector parallel to the wave normal with length equal to the refractive index. The variable \mathbf{v} is a unit vector and parallel to the local magnetic field. The variable p can be derived from the cold plasma approximation-based Altar-Appleton-Hartree dispersion relation (Appleton, 1928, 1932; Hartree, 1931; Stix, 1992). In the differential equations, term $\frac{dx_i}{dt}$ represents the variations of ray positions with respect to time, and $\frac{du_i}{dt}$ gives the wave vector variations along the raypath. The Artemis-P code employs a fourth order Runge-Kutta algorithm to solve these differential equations. An important note concerning the ray-tracing method is that this code does not incorporate a reflection mechanism, as implementing reflection would require reversing the integration direction (raypath direction) at the point of reflection, which is a challenging determination (Haselgrove, 1963). Nevertheless, in the majority of cases, the rays exhibit behavior similar to reflection, as they effectively undergo continuous refraction when propagating toward the cut-off surface due to the rapid variation of the refraction index. If the angle of incidence on an interface or density gradient led to wave reflection, the code would stop, and the rays would terminate at that point. For this reason, we refer to these “refracted” and “terminated” rays as “reflected” rays, although this phenomenon is rarely observed in the simulations.

To adapt the Artemis-P code to Saturn's plasma environment, we constructed the electron density model by merging various existing models (Persoon et al., 2006, 2019, 2020), as depicted in Figure 1. Panel (a) displays the scale height plasma torus model by Persoon et al. (2006), designed for latitudes up to 20° and ranging from $L = [3.6 \sim 8.6]$ (L-Shell corresponds to the distance, normalized to the planetary radius, of a dipolar field line apex in the equatorial plane; McIlwain, 1966). This model enables us to extrapolate values to higher latitudes and larger L shells because of its rapid electron density decrease beyond the plasma torus region, making it suitable for providing electron density estimates outside the plasma torus. Panel (b) illustrates the diffusive equilibrium model of the plasma torus by Persoon et al. (2020), employed here for determining the electron density of the plasma torus. This model captures finer structures at the outer boundary of the plasma torus if compared to the scale-height model shown in Panel (a), valid for latitudes up to approximately 30° and L values ranging from 2.4 to 10. In the case of the ionosphere model by Persoon et al. (2019) presented in Panel (c), only the northern hemisphere profile was utilized to avoid introducing large density gradients due to north-south asymmetry. The ray-tracing calculations were exclusively conducted in the northern hemisphere.

Figure 1 Panel (d) shows the merging of these three models with the connection regions between these models removed. To smoothly fill these white connection regions with density values and ensure monotonic variations, we employ an inpainting algorithm based on least-square estimation (Crema et al., 2020) that is frequently used for topographic data reconstruction in geomorphology and ecology. The resulting electron density was presented in Panel (e). Furthermore, we constructed a magnetosheath using the magnetopause model by Kanani et al. (2010) and the bow shock model by Went et al. (2011), considering a solar wind dynamic pressure of 0.036 nPa, which is a typical value measured at 9.5 AU (Echer, 2019; Jackman & Arridge, 2011).

The electron density within the magnetosheath is derived using the Rankine-Hugoniot relation, which provides the relationship between solar wind parameters (velocity, temperature, density) upstream and downstream of the

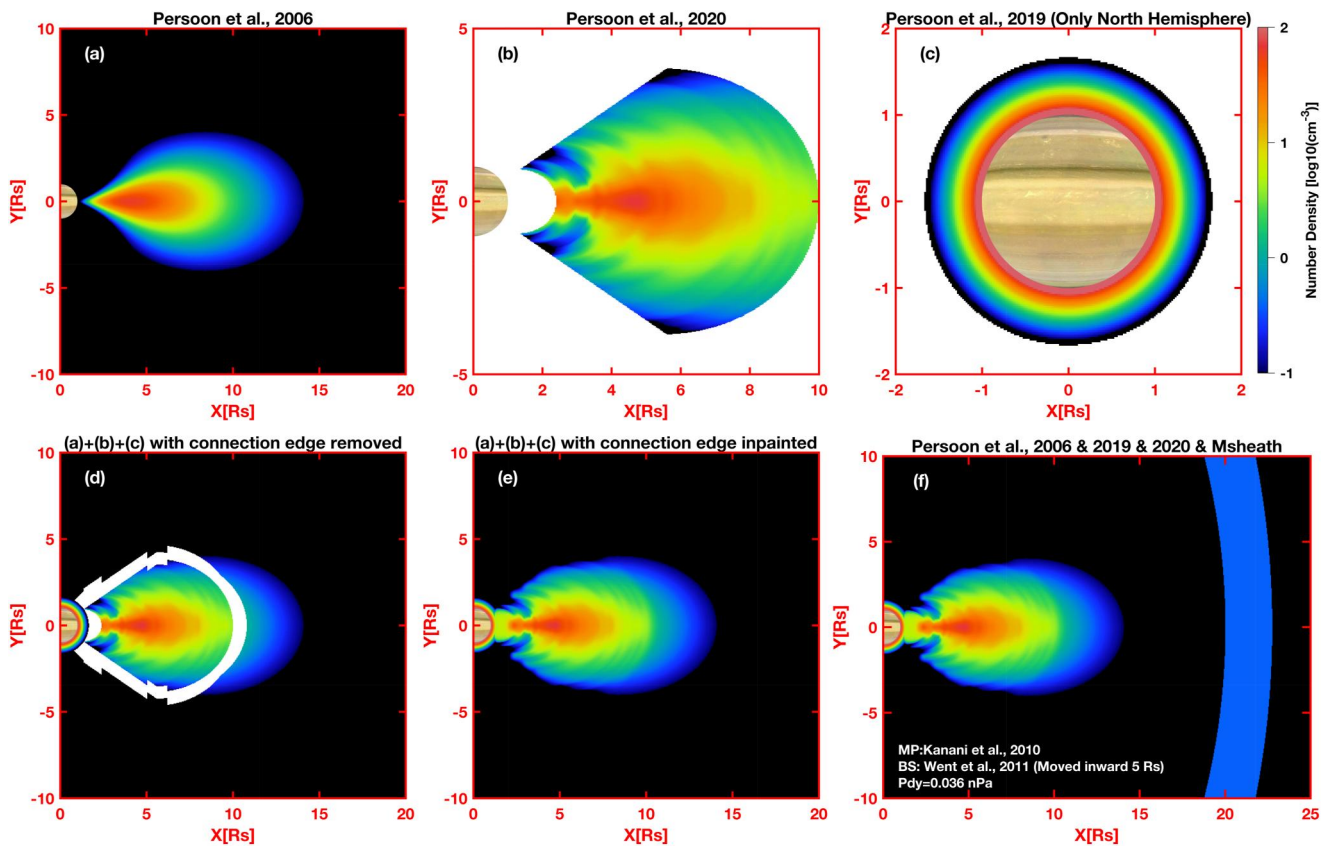


Figure 1. Construction of Saturn's electron density environment. Panels (a)–(c) display the plasma torus models of Persoon et al. (2006 & 2020) and the ionosphere model of Persoon et al. (2019). Panel (d) presents the merged result of the three models in Panels (a)–(c), with the connection regions between these models removed (highlighted in white color). Panel (e) displays the algorithm derived electron density model from Panel (d). The magnetosheath is added into the model as illustrated in Panel (f) using the magnetopause and bow shock model with solar wind dynamic pressure $P_{dy}=0.036 \text{ nPa}$. The electron density inside the magnetosheath is determined based on the Rankine-Hugoniot relation and remains mostly constant in the modeled region.

collisionless shock. By combining the shock geometry from the model of Went et al. (2011) and the upstream solar wind parameters, the electron number density downstream of the bow shock within the magnetosheath can be determined. We assume typical solar wind parameters near Saturn (Echer, 2019): 90° angle between the interplanetary magnetic field and shock normal, interplanetary magnetic field strength = 0.48 nT , solar wind density = 0.098 cm^{-3} , solar wind speed = 430 km/s , and solar wind flow direction along the $-X$ axis (horizontal axis in Figure 1 Panel (f)). We derive the magnetosheath electron density along the Y direction (vertical axis in Figure 1 Panel (f)). The magnetosheath electron density remains nearly constant within the modeled range, as shown in Figure 1 Panel (f), with a minimum electron density $>0.3 \text{ cm}^{-3}$ (corresponding to a local $f_{pe} \geq 5 \text{ kHz}$). Note that for clarity, the size of the magnetosheath is reduced in the calculation with the bow shock shifted inward by 5 Rs (Saturn Radii = $60,268 \text{ km}$), as depicted in Figure 1 Panel (f). The magnetic field model used was from Dougherty et al. (2018). The final adapted magnetic field and electron density profiles at Saturn are presented in Figure 2.

3. Observations of Saturn Narrowband Emissions

A typical Cassini observation of NB emissions is depicted in Figure 3, Panel (a). The NB emissions, characterized by frequencies near 5 and 20 kHz , are evident in the spectrogram. At 11 July and near $12:00 \text{ UT}$, Cassini is in the dayside magnetosheath (inferred from the boundary crossing list of Jackman et al., 2019) as marked by the text in Panel (a). The 5 kHz NB emission shows a cut-off at the magnetopause, whereas the 20 kHz NB emissions can propagate into the magnetosheath with some attenuation, as previously discussed in Wu et al. (2022). The observations shown in Figure 3 Panels (a)–(b), including the wave electric field spectrogram and circular polarization, were obtained from measurements of the Cassini RPWS (Radio and Plasma Wave Science) High

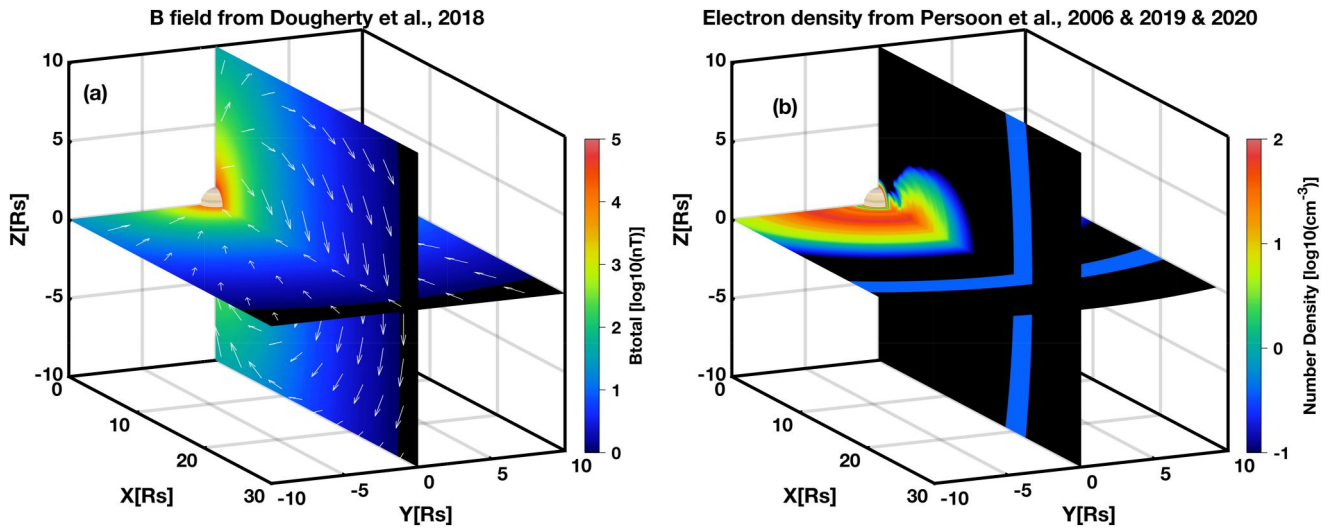


Figure 2. Illustration of the magnetic field and the constructed electron density model at Saturn. Panel (a) displays Saturn's magnetic field model with the white arrows indicating the direction of the magnetic field (Dougherty et al., 2018). The color-code represents the strength of the magnetic field. Panel (b) presents the constructed electron density model.

Frequency Receiver (Gurnett et al., 2004). Circular polarization data were derived using the method of Cecconi and Zarka (2005).

The circular polarization (Stokes parameter V) in Panel (b) is determined by assuming pure circular polarization with no linear polarization ($Q = U = 0$; Cecconi & Zarka, 2005). By examining the circular polarization, the wave magnetoionic mode can be identified. For example, L-O mode emissions can only propagate in regions where the wave frequency exceeds the local f_{pe} and exhibit left-hand circular polarization ($V > 0$ in the northern hemisphere and $V < 0$ in the southern hemisphere in the data due to distinct magnetic field orientations in the two hemispheres). The identified L-O mode NB emissions are indicated by the black arrows in Panel (b). Z mode waves propagate both below and above f_{pe} with an opposite sense of polarization. These Z mode waves are trapped roughly in the region highlighted by red text below Panel (b) and indicated by the green and pink arrows in Panels (c)–(d).

Figure 3 Panels (c)–(d) provide the trajectory (black line) of Cassini during the time interval of Panel (a), with the observed Narrowband (NB) emissions (indicated by the black, green, and pink arrows in Panel (b)) marked by black (L-O mode), green (Z_{R-X} mode), and pink (Z_{L-X} mode) squares along the trajectory. As identified and indicated by the black arrows in Panel (b), the majority of the NB emissions are observed to be L-O mode emissions. In Panels (c)–(d), the Z mode trapping regions are analytically determined by utilizing the magnetic field and electron density model as described in Section 2. The Z mode TR can be further divided into two regions: TR-1 with $f_{pe} < f_{wave} < f_{lh}$ (corresponding to Z_{R-X} mode, indicated by the green arrow in Panels (c)–(d)) and TR-2 with $f_{pe} > f_{wave} > f_z$ (corresponding to Z_{L-X} mode, indicated by the pink arrow in Panels (c)–(d)). These frequency surfaces are derived from the magnetic field and electron density model by calculating these characteristic frequencies at 5 and 20 kHz. TR-1 for Z_{R-X} mode waves is relatively extensive, delimited by the f_{lh} surface and f_{pe} surface, while TR-2 for Z_{L-X} mode waves is narrow, constrained by f_{pe} and f_z surfaces along the edge of the plasma torus. As illustrated by the characteristic frequency lines in Panels (c)–(d), the TR for 20 kHz NB emissions is much smaller than the 5 kHz TR due to the higher wave frequency.

It is evident that the 5 kHz Z_{R-X} mode (green squares in Panel (c)) waves are observed within the TR-1 ($f_{pe=5\text{ kHz}} < f_{wave} < f_{lh=5\text{ kHz}}$, indicated by the green text), which is consistent with the theoretical prediction and suggests these frequency surfaces well represent the plasma environment around the TR-1. The 5 kHz Z_{L-X} mode events (pink squares in Panel (c)) are observed near TR-2 ($f_{pe=5\text{ kHz}} > f_{wave} > f_z=5\text{ kHz}$, indicated by the pink text) but are not exclusively restricted to TR-2, indicating a more complex plasma environment than our meridional model can account for. A detailed analysis of this event including local estimates of f_{pe} from Langmuir probe measurements is presented in Woodfield et al. (2018). Due to the uncertainty of the measured plasma

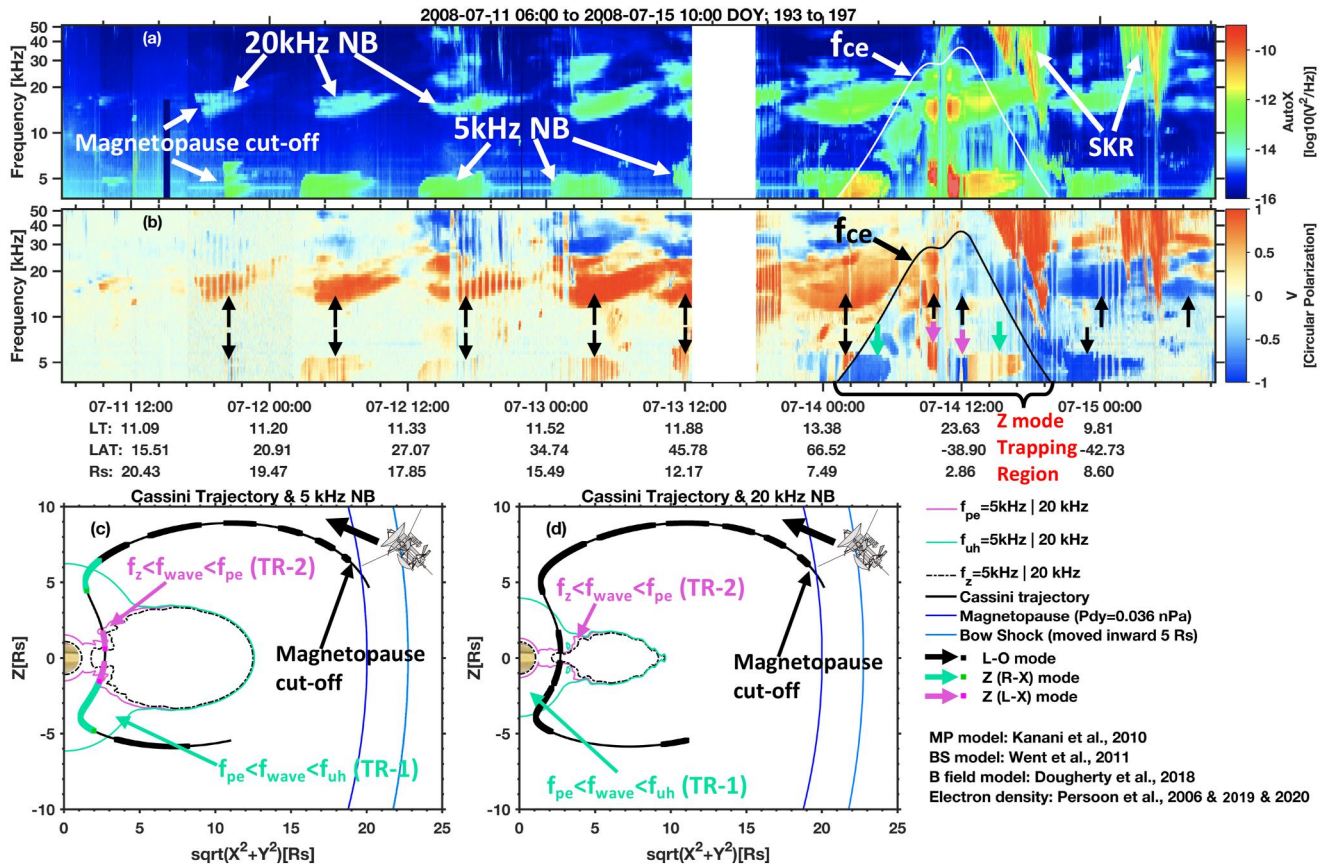


Figure 3. Observation examples of Saturn Narrowband emissions during an interval from 2008-07-11 6:00 to 2008-07-15 10:00. Panels (a)–(b) present the spectrogram of the Cassini Radio and Plasma Wave Science (RPWS) electric field intensity, as well as the circular polarization (Stokes parameter V) determined by the inversion method of Cecconi and Zarka (2005). The arrows in Panel (b) indicate the different modes of NB emissions: black for L-O mode, green for Z_{R-X} mode, and pink for Z_{L-X} mode. The white and black curves in Panels (a)–(b) represent the local f_{ce} . The intensity modulation of the spectrogram (vertical stripes) near 07-11 22:00 and 07-12 18:00 is due to the rolling of Cassini spacecraft. Panels (c)–(d) illustrate the Cassini orbit in the meridional plane during the time interval of Panel (a). The overlapping black, green, and pink squares along the trajectory of Cassini denote the locations where the 5 kHz and 20 kHz NB emissions (in Panel (a)) are observed in L-O mode, Z_{R-X} mode, and Z_{L-X} mode, respectively. The contour lines (f_{pe} (pink), f_z (black dashed), f_{uh} (green)) in Panels (c)–(d) are derived using the magnetic field and electron density model described in Section 3. Additionally, the blue lines mark the locations of the magnetopause and bow shock, obtained from the model of Kanani et al. (2010) and Went et al. (2011), considering a typical solar wind dynamic pressure at Saturn, $Pdy = 0.036$ nPa (Jackman et al., 2011; Echer, 2019).

parameters during this time interval, all 20 kHz NB emissions observed are identified as L-O mode emissions and marked as black squares in Panels (b) and (d).

Figure 3 presents typical observation patterns of Saturn NB emissions, where L-O mode waves are commonly observed away from the equatorial region, while Z mode emissions are prevalent when Cassini approaches the region near Saturn, below the f_{ce} lines in Panels (a)–(b). In summary, the distributions of the different modes of NB emissions are described. The later ray-tracing calculations for the L-O mode and Z mode NB emissions are conducted in the relevant propagation region.

4. Source Region of Saturn Narrowband Emissions

The initial conditions for ray-tracing calculations in terms of source positions and initial WNAs of rays are based on several theoretical studies on the generation mechanism of NB emissions. These are discussed in the following.

The frequently observed L-O mode NB emissions (at both 5 and 20 kHz bands) are mode converted from the Z mode waves near the density gradients at the boundary of the plasma torus (Menietti et al., 2016, 2019; Ye, Menietti, et al., 2010). This mode conversion takes place when Z mode waves propagate to density gradients with a WNA close to 0° and the local f_{pe} matches the wave frequency (Ellis, 1956; Menietti et al., 2016), that is, $f_{pe} = 5$ kHz & 20 kHz.

Table 1
Summary of the Proposed Generation Mechanisms of Z Mode Narrowband Emissions

NB emissions	Previous works	Mechanism	Z mode WNA	f_{pe}/f_{ce} ratio at sources
5 kHz	Menietti et al. (2016)	CMI operating at $f_{pe}/f_{ce} < 1$	$\cong 0^\circ$	$f_{pe}/f_{ce} \cong 0.21$
20 kHz	Menietti et al. (2009, 2010, 2019)	CMI operating at $f_{uh} = nf_{ce}$ ($n = 2 \sim 6$)	$> 80^\circ$	$f_{pe}/f_{ce} = [1.4 \sim 5.9]$
	Ye et al. (2009)	UHW: Mode conversion from enhanced upper hybrid waves when $f_{uh} = (n + \frac{1}{2})f_{ce}$, ($n = 1 \sim 5$)	highly oblique $\cong 90^\circ$	$f_{pe}/f_{ce} = [1.1 \sim 2.7]$

Previous studies have proposed two generation mechanisms for Z mode NB emissions. One related mechanism is the cyclotron maser instability (CMI) operating under a certain range of plasma conditions (Wu & Lee, 1979; Yoon et al., 1996, 1998). For instance, Menietti et al. (2016) found that the 5 kHz Z mode waves are generated within sources with $f_{pe}/f_{ce} \cong 0.21$, and the maximum Z mode growth rate occurs at WNA $\cong 0^\circ$. This result aligns with the calculations of Melrose et al. (1984), indicating that the Z mode growth rate becomes dominant when $0.3 < f_{pe}/f_{ce} < 1.3$. Additionally, when f_{pe}/f_{ce} values become larger and meet the condition $f_{uh} = nf_{ce}$ ($n = 2, 3, 4, 5, 6$, equivalent to $1.4 < f_{pe}/f_{ce} < 5.9$), the so-called Z mode maser mechanisms come into play, generating Z mode waves with $f_{wave} = f_{uh} = nf_{ce}$ (Yi et al., 2013; Yoon et al., 1996, 1998). This mechanism is proposed for the 20 kHz Z mode emissions, and the maximum growth rate calculated within the possible source regions occurs at WNA $\cong 90^\circ$ (Menietti et al., 2009, 2010, 2019). We refer to the CMI mechanisms as CMI in subsequent discussions. Note that due to the low resolution of particle measurements by Cassini, previous works on the growth rate calculations relied heavily on assumptions about the observed electron distribution. As a result, the true picture of the generation mechanism is still under investigation.

The second mechanism for the Z mode NB emissions is proposed by Ye, Menietti, et al. (2010), suggesting that the enhanced upper hybrid waves could be responsible for generating the Z mode waves. When the condition $f_{uh} = (n + 1/2)f_{ce}$ is met, the enhanced upper hybrid waves may convert into Z mode waves (Gurnett et al., 1981; Kurth, Ashour-Abdalla, et al., 1979, Kurth, Carven, et al., 1979). Observations in Ye et al. (2009) support this mechanism for the 20 kHz Z mode waves. However, for the 5 kHz Z mode waves, there are scarce observations of the upper hybrid waves in the frequency range near 5 kHz. This lack of observation could be due to the sensitivity limitations of the 10-m monopoles of the Cassini RPWS instrument. The dipole of the RPWS instrument consists of two monopole arms, which are each 10-m in length (Gurnett et al., 2004). The wavelength of these electrostatic waves near 5 kHz, which is proportional to the local λ_D (where λ_D is the Debye length), can be much larger than the antenna length, leading to sensitivity issues in detecting these waves with RPWS to detect these upper hybrid waves near 5 kHz (Gurnett, 1998, 2020). In subsequent discussions, we refer to the generation mechanism of Z mode from the enhanced upper hybrid waves as UHW. Table 1 provides a summary of these previous works on the generation mechanisms of Z mode NB emissions.

In Menietti, Averkamp, Ye, Sulaiman, et al. (2018), whistler mode NB emissions at the 5 kHz band were observed when Cassini crossed Saturn's equatorial ionosphere inside the inner region of the plasma torus during Cassini's last year orbits. The presence of whistler mode emissions at 5 kHz and possibly at 20 kHz is restricted to regions where the f_{wave} is smaller than the local f_{pe} or f_{ce} , whichever is lower. These regions are located inside the plasma torus and in close proximity to Saturn (see Figure 4 for details), where Cassini had limited orbital coverage. The whistler mode NB emissions may also arise from mode conversion of Z mode emissions at density gradients on the f_{pe} surface (Ellis, 1956; Yoon et al., 1998), propagating with small WNAs along the magnetic field lines. However, due to the limited observations, there has been no further investigation into these emissions. Therefore, this work only gives an estimation of the whistler mode propagation zones and no ray-tracing calculation is carried out due to the lack of observation.

Based on the aforementioned studies, we have distinguished potential source regions for L-O mode, Z mode, and whistler mode NB emissions using the constructed electron density and magnetic field model shown in Figure 3. The sources for L-O mode NB emissions at both 5 and 20 kHz are identified along the f_{pe} surfaces with $f_{pe} = 5$ and 20 kHz, as indicated by transparent blue dots in Figure 4 Panels (a) and (d) (shown as blue dots or thick blue lines due to the overlapping of the dots). The extension of the L-O mode sources along the f_{pe} contour line to the outer

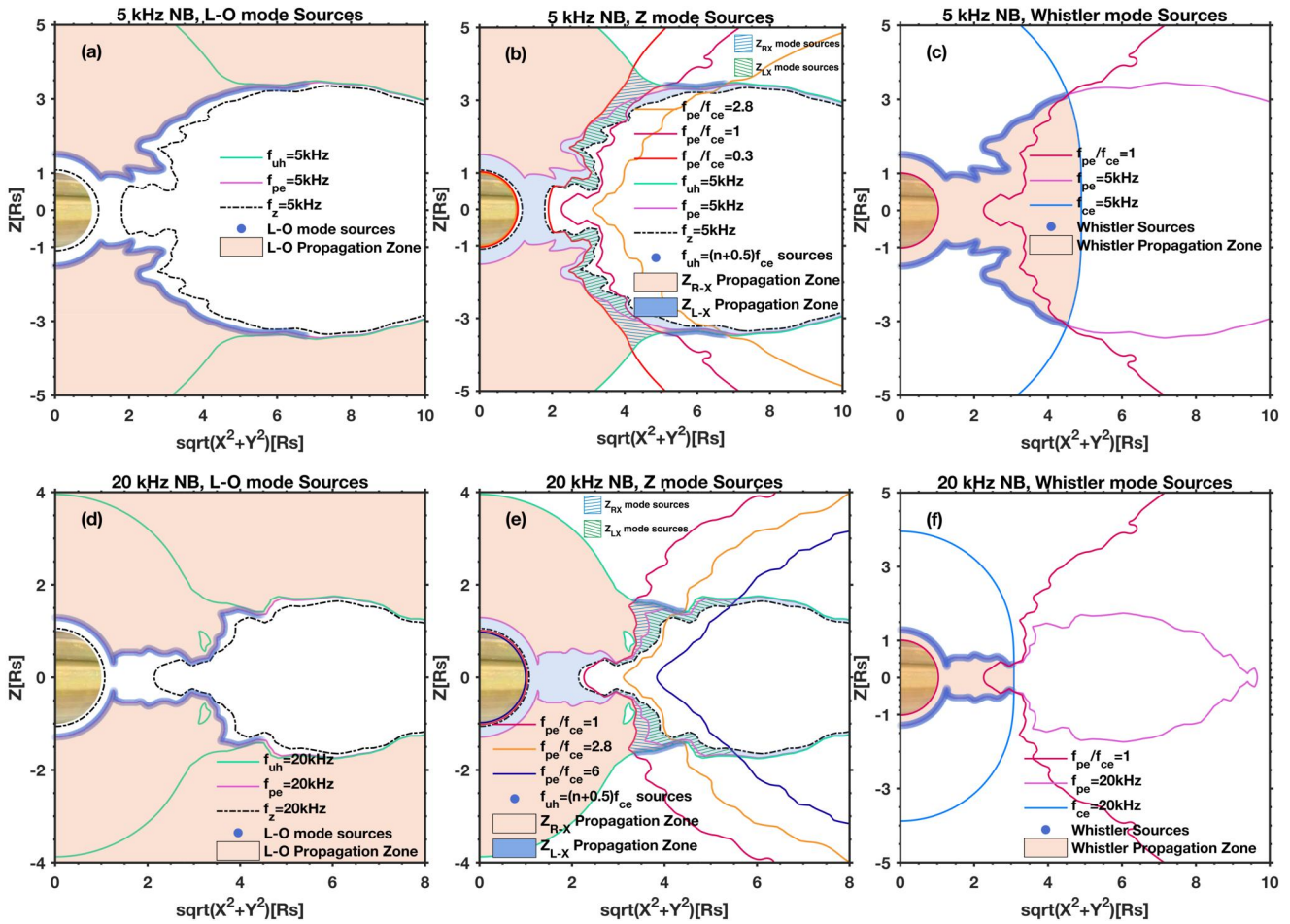


Figure 4. The source regions of Saturn NB emissions. In Panel (a), the possible source region of 5 kHz L-O NB emissions is represented by blue dots (or as thick blue lines due to the overlapping of the dots) along the f_{pe} contour line, assuming mode conversion from Z mode waves there. The orange color indicates the region where these emissions can propagate. Panel (b) displays the possible source region of 5 kHz Z mode NB emissions, with three source regions denoted by blue and green shading and blue dots. Contour lines for f_{uh} , f_z , f_{pe} , and $f_{pe}/f_{ce} = 0.3, 1, 2.8$ are derived from the constructed electron density and magnetic field model. The propagation zone of Z mode waves is marked by the orange (TR-1) and light blue (TR-2) regions. Panel (c) shows the possible source region of 5 kHz whistler mode NB emissions as marked by the blue dots along f_{pe} lines. The propagation zone of whistler mode emissions is indicated by the orange region. Panels (d)–(f) demonstrate the possible sources for 20 kHz NB emissions in a similar format to Panels (a)–(c).

part of the plasma torus is restricted to the $f_{uh} = 5$ and 20 kHz surfaces due to the trapping of Z mode waves within the f_{uh} contour lines. The propagation zones, where L-O mode NB emissions can travel, are color-shaded in orange in Panels (a) and (d).

Figure 4 Panel (b) identifies the 5 kHz Z mode wave sources using the cyclotron maser instability (CMI) theory with the ratio of f_{pe}/f_{ce} ranging from 0.3 (red line) to 1 (dark red line), and within the region bounded by the f_{uh} (cyan line) and f_z (black dashed line) contour lines based on the previous studies and summarized in Table 2. These lines encircle two distinct regions separated by the f_{pe} line, falling within TR-1 for Z_{RX} mode emissions and TR-2 for Z_{LX} mode emissions, as indicated by the grid shaded area. Additionally, we examine the possible UHW sources for the 5 kHz Z mode Narrowband (NB) emissions (shown as blue dots or thick blue lines) along the f_{uh} contour line when condition $1 < f_{pe}/f_{ce} < 2.8$ is met. For 20 kHz Z mode NB emissions (in Panel (e)), the source regions are determined using both CMI and UHW parameters, requiring $1 < f_{pe}/f_{ce} < 6$ for CMI parameters and $1 < f_{pe}/f_{ce} < 2.8$ for UHW parameters along the f_{uh} line based on the previous studies. The UHW sources (indicated by blue dots in Panel (e)) align with the source region predicted by CMI, as demonstrated in Panel (e). As will be detailed in Section 6, rays initiated along the f_{uh} line become trapped within these source regions quickly. Consequently, we explore an extended scenario of the source regions, extending the source regions to the inner boundary of the

Table 2
Ray-Tracing Parameters of the Source Regions and Initial Propagation Angle of Narrowband Emissions

NB emissions	Wave mode	Source location	Launch WNA
5 kHz	O	Source close to f_{pe} line and within Z mode trapping region	180° (northern hemisphere)
	Z	CMI (Melrose et al., 1984; Menietti et al., 2016): (1) $f_{pe}/f_{ce} = [0.3 \ 1]$ (2) $f_z < f_{wave} < f_{uh}$	0° & 180°
		UHW (Ye et al., 2009): (1) $f_{pe}/f_{ce} = [1 \ 2.8]$ (2) $f_{wave} \cong f_{uh} = (n + \frac{1}{2})f_{ce}$	70° & 80° & 90° & 100° & 110°
20 kHz	O	Source close to f_{pe} line and within Z mode trapping region	180° (northern hemisphere)
	Z	CMI (Menietti et al., 2009, 2010, 2019): (1) $f_{pe}/f_{ce} = [1 \ 6]$ (2) $f_z < f_{wave} \leq f_{uh}$	90° & 270°
		UHW (Ye et al., 2009): (1) $f_{pe}/f_{ce} = [1 \ 2.8]$ (2) $f_{wave} \cong f_{uh}$	70° & 80° & 90° & 100° & 110°

plasma torus (outlined by the grid shaded region). This extended region still satisfies condition $1 < f_{pe}/f_{ce} < 6$, although it diverges from the f_{uh} line. The trapping regions (propagation zones) of Z mode waves are color-shaded in Panels (b) and (e), with TR-1 in orange and TR-2 in light blue.

Although this study did not calculate the raypath of the whistler mode emissions, the possible source region and propagation zone were identified using the constructed model (Panels (c) and (f)). Whistler mode NB emissions can propagate into the region between the inner part of the plasma torus and the planet, suggesting the possibility of emissions traversing from one hemisphere to the other through the whistler mode. It should be noted that in the TR-2 region (light blue shaded areas in Panels (b) and (e)), Z_{LX} mode emissions can also cross the equator from the region between the inner part torus and the planet, as constructed from the algorithm described in Section 2.

Once the source region of the NB emissions is determined, rays are launched from the identified region with specific initial WNAs, as summarized in Table 2 based on previous studies. The initial WNAs for L-O mode NB emissions are set to be parallel to the background magnetic field (anti-parallel in the northern hemisphere, WNA = 180°). For Z mode emissions at both 5 and 20 kHz, CMI rays are launched with theoretical WNAs from previous studies (0° & 180° for 5 kHz Z mode, 90° & 270° for 20 kHz Z mode), while UHW rays are launched with larger WNAs ranging from 70° to 110° with a stepping of 10°.

5. Propagation of the L-O Mode Narrowband Emissions

The L-O mode NB emissions at both frequency bands are launched anti-parallel to the background magnetic field along the $f_{wave} = f_{pe}$ contours, as shown by the pink lines in Figure 5 Panels (a) and (d).

In Figure 5 Panel (a), the propagation pattern of the 5 kHz L-O mode NB emissions is displayed, showing reflections and multi-reflections between the ionosphere, magnetosheath, and the plasma torus. Observations by Wu et al. (2021) suggested that a certain proportion of 5 kHz L-O NB emissions can be reflected in the equatorial region outside the plasma torus. However, our calculations suggest that rays reach these regions only rarely, possibly due to the smooth magnetopause boundary considered in this study. This highlights the importance of small-scale density structures, such as Kelvin-Helmholtz instability vortices (Burkholder et al., 2020; Ma et al., 2022), for the propagation of L-O mode NB emissions near the magnetosheath. The KHI-generated electron density structures will further influence the reflection direction of the waves near the magnetopause, either toward low or high latitudes, back toward the lobe, the planet, or the plasma torus. Panel (a) also demonstrates the tendency of the 5 kHz L-O mode NB emissions launched along the inner edge of the plasma torus to propagate toward or reflect higher latitudes. Moreover, magnetosheath reflection enables emissions to traverse the magnetosphere, allowing the propagation of O mode emissions from one side of the planet (e.g., duskside) to the other side (e.g., dawnside). The shape of the edge of the plasma torus and its small-scale structures also cause the rays to be reflected on the other side of the planet. The electron density model of Persoon et al. (2020) presents “slot” or “trough” regions with lower electron density in the north-south inner edge of the plasma torus near Saturn, which tend to trap the L-O mode waves. Multi-reflections inside this slot region are observed in the zoomed-in view of Panel (a) in Panels (b)–(c). These multi-reflections, caused by the slot region, can effectively explain the depolarization features of the NB emissions in this area, as observed in the statistical study by Wu et al. (2021).

The 20 kHz L-O mode NB emissions exhibit reflections at the ionosphere and plasma torus, as seen in Figure 5 Panel (d). Unlike the 5 kHz emissions, which are reflected by the magnetosheath, the 20 kHz rays can pass

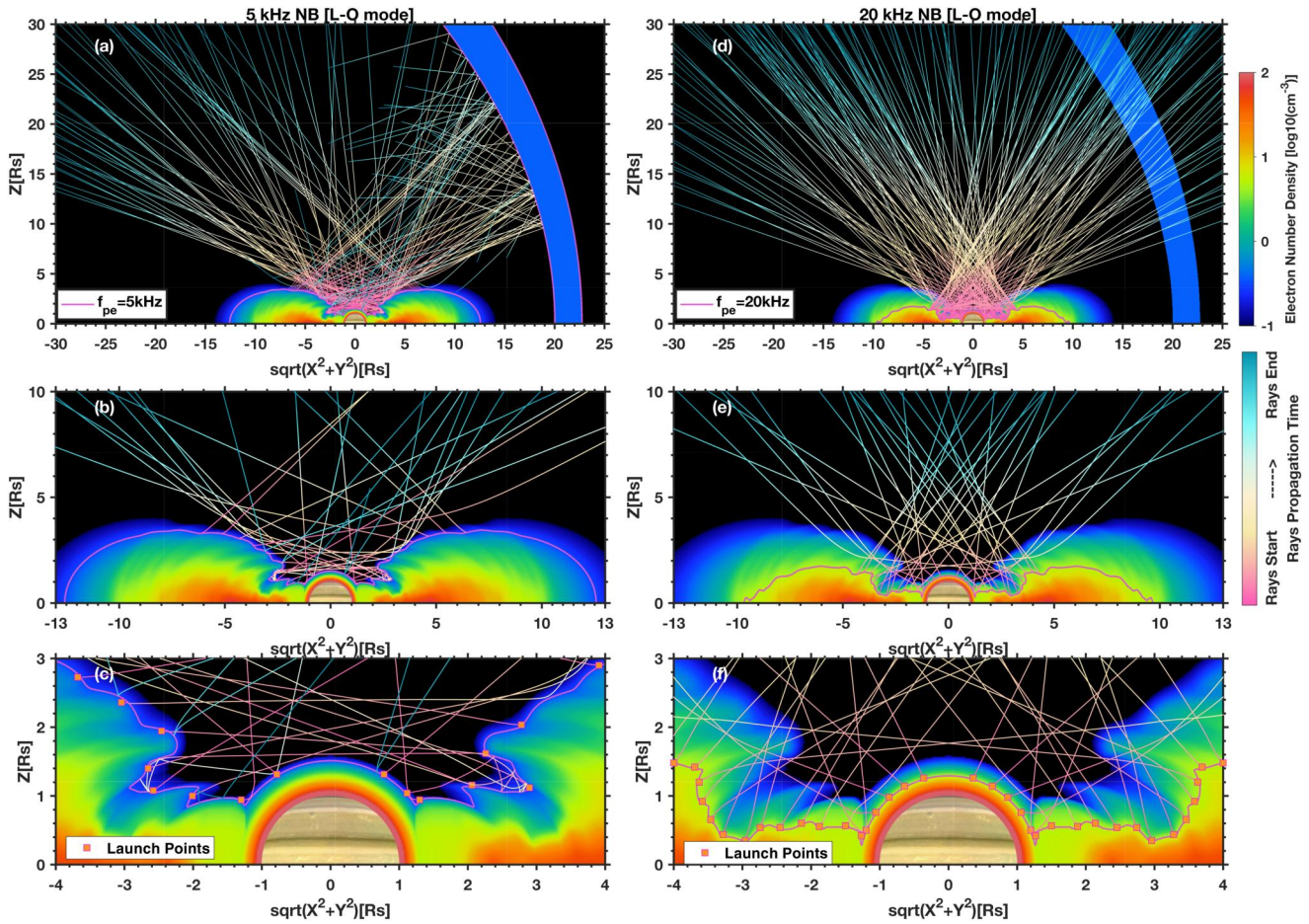


Figure 5. L-O mode Narrowband (NB) propagation within the Saturnian magnetosphere. Panel (a) shows the propagation paths of 5 kHz NB emissions in the meridional plane, with the initial wave normal angle restricted to 180° . The background color-code represents the electron density, while the color along the raypath indicates the ray start location (pink) and the ray end location (cyan). Panels (b)–(c) offer a zoomed-in view of Panel (a) specifically near Saturn, with only a subset of rays displayed. The launch points of the rays are marked by pink squares in Panel (c). Panels (d)–(f) present the results for 20 kHz NB emissions using the same format as Panels (a)–(c).

through the magnetosheath and escape from the magnetosphere due to the lower electron density in that region as shown in Figure 3, albeit with some attenuation. Sometimes, 5 kHz NB emissions can also traverse the magnetosheath when the electron density is low enough. The “slot” region for the 20 kHz emissions, formed by the $f_{pe} = 20$ kHz contour line, appears more “open” compared to the 5 kHz “slot” region. Although theoretically, the 20 kHz L-O NB emissions could be trapped within the slot region under appropriate propagation angles, our calculations in Panels (d)–(f) show that all rays propagate outward from the slot region and are reflected at the ionosphere, hence no “trapping” is observed.

6. Propagation of the Z Mode Narrowband Emission

The Z mode NB emissions at the two frequency bands are launched using CMI parameters, with the initial WNA parallel (both at 0° and 180°) to the background magnetic field for the 5 kHz Z mode and perpendicular (both at 90° and 270°) to the magnetic field for the 20 kHz, as shown in Figure 6. Panel (a) provides the overall propagation pattern of the 5 kHz Z mode NB emissions within the TR using CMI source parameters. Z mode waves stop when they encounter the f_{ih} surface, leading to resonance as indicated by cyan colors on the raypaths near the f_{ih} surface. Reflections of Z mode waves occur at the ionosphere and the inner boundary of the plasma torus, where the Z mode reaches the f_z frequency surface. Similar to the 5 kHz L-O mode emissions, the Z mode waves also exhibit a trapping tendency (multi-reflections) in the “slot” region near the boundary of the plasma torus, as shown by the zoom-in views in Panels (b)–(c). As shown in Figure 4 Panel (b), the Z mode rays are launched at both the Z_{RX} source region (within TR-1 with $f_{wave} > f_{pe}$) and the Z_{LX} source region (within TR-2 with $f_{wave} < f_{pe}$).

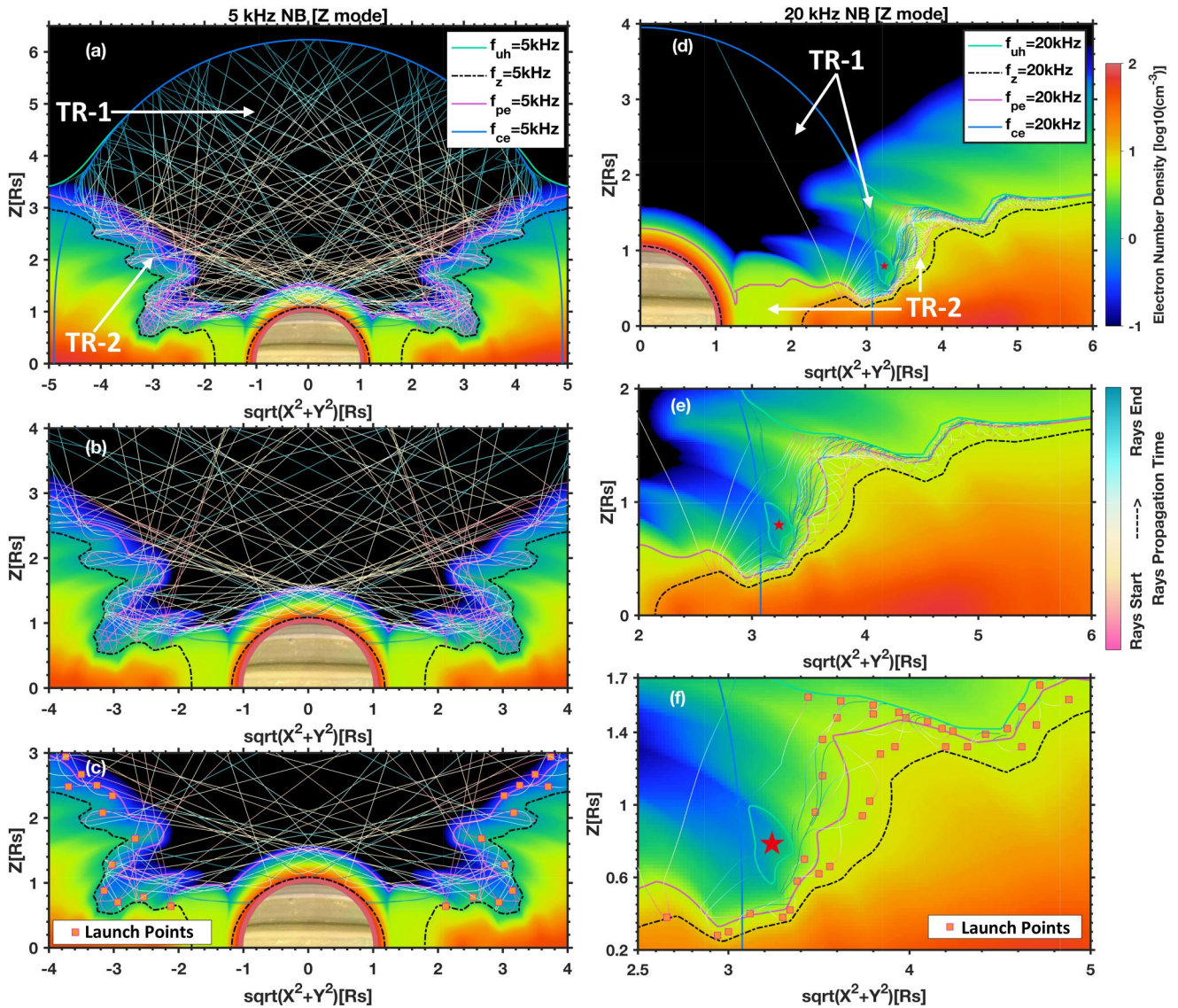


Figure 6. Z mode Narrowband (NB) propagation within the Saturnian magnetosphere using the cyclotron maser instability source parameters. In Panel (a), the propagation paths of the 5 kHz Z mode NB emissions are shown in the meridional plane, with the initial wave normal angle restricted to 0° and 180° . Panels (b)–(c) provide a zoomed-in view of Panel (a) near Saturn, with only selected rays displayed. The launch point of the rays is indicated by a pink square in Panel (c). Similar results for the 20 kHz Z mode NB emissions are presented in Panels (d)–(f) in the same format as Panels (a)–(c). The solid green, pink, blue and black (dashed) lines represent the f_{uh} , f_{pe} , f_{ce} , and f_z frequencies for 5 kHz (Panels (a)–(c)) and 20 kHz (Panels (d)–(f)), respectively. The background color-code represents the electron density in the same format as Figure 5. The red star symbols in Panels (d)–(f) indicate a local f_{uh} cavity.

The Z mode waves experience a change in propagation direction as they cross the f_{pe} surface due to the variation in the refractive index near f_{pe} . The f_{pe} surface is also where mode conversion from Z mode to L-O mode or whistler mode waves occurs, connecting the L-O mode rays in Figure 5 and Z mode waves in Figure 6. However, a detailed analysis of the mode conversion processes near the plasma torus boundary cannot be resolved by the ray-tracing code based on the cold plasma approximation. This requires further investigation using full electromagnetic treatment, as well as including sharper density gradients than provided by our current model, which is why we leave this problem for a future study.

The source regions for the 20 kHz Z mode NB emissions are suggested to be located at the north-south edges of the plasma torus, as shown in Figure 4 Panel (e). These rays in Figure 6 Panels (d)–(f) are launched within the source regions with initial WNAs of 90° and 270° within the meridional plane, both perpendicular to the magnetic field direction. However, as depicted in Figure 6 Panel (d), the 20 kHz Z mode rays tend to remain trapped near

the source region and do not propagate far. This behavior is attributed to the proximity of the sources to the f_{uh} and f_z surfaces, where the rays quickly get into resonance or face their cut-off, respectively. Panels (d)–(f) also reveal the presence of a small f_{uh} cavity in the model (indicated by the red star symbols), which stops all Z mode rays upon reaching the f_{uh} surface. This cavity is not a technical artifact in the construction of the electron density model, but rather a result of the relatively low electron density in the “slot” region. Consequently, the 20 kHz Z mode rays struggle to escape from the narrow source regions formed by the f_{uh} and f_z surfaces at the north-south edges of the plasma torus.

The difficulties faced by the 20 kHz Z mode rays in propagating inward to escape from the source region can be attributed to another reason. As depicted in Figure 6 Panel (f), some rays stop near either the f_{ce} or f_{pe} surfaces and never reach the f_{uh} surface. This is because these Z mode rays reach the resonance frequency at f_{ci} when they propagate to either the f_{pe} or f_{ce} surface with smaller WNAs. This resonance is dependent on the background plasma environment, where $f_{pe}/f_{ce} > 1$ leads to $f_{ci} \cong f_{pe}$, and $f_{pe}/f_{ce} < 1$ results in $f_{ci} \cong f_{ce}$. In Panel (f), the region above the f_{uh} cavity (indicated by the red star symbol) have $f_{pe}/f_{ce} < 1$, causing the rays to stop near f_{ce} as the rays propagate with small WNAs. However, below the f_{uh} cavity, some Z mode rays can cross the f_{ce} due to their larger WNAs. In more realistic scenarios, with highly variable magnetic fields and plasma torus conditions, these Z mode rays would still have opportunities to escape from their source regions.

We also present the raypaths of Z mode NB emissions using the UHW source parameters, with the rays launched close to the f_{uh} surfaces where the conditions in Table 2 are satisfied, spanning a range of WNA from 70° to 110° , as shown in Figure 7. The results closely resemble those in Figure 6 Panels (d)–(f), with the rays quickly reaching resonance near the resonance frequency. For the 5 kHz Z mode emissions (Panels (a)–(c)), the rays are reflected at different layers before reaching the f_z surface due to varying incident angles. Similarly, for the 20 kHz Z mode NB emissions, the source regions derived from the UHW mechanism are in close proximity to the CMI theory, and the propagation pattern shows the emissions predominantly trapped near the source regions.

7. Propagation of the L-O Mode and Z Mode Emissions With Arbitrary Angles

To overcome the limitations imposed by selected source positions and initial WNAs, we conducted additional tests by launching rays within the propagation zones of each corresponding wave mode in both the longitudinal and azimuthal directions. This approach allowed us to explore potential raypaths under highly dynamic magnetospheric conditions, as shown in Figures 8 and 9.

The computational results for the L-O mode emissions at both frequency bands are showcased in Figure 8. To explore potential ray trajectories comprehensively, we launched 35 rays within both a meridional and a horizontal plane, encompassing full launch circles of 360° .

Similar to the results in Figure 5, the L-O mode waves propagate along nearly straight paths but experience reflections at strong density gradients, such as the ionosphere, magnetosheath, and the plasma torus, as depicted in Panels (a)–(d). Additionally, in Figure 8 Panels (e)–(f), new calculations are shown with the L-O mode rays launched in the initial direction toward the azimuthal direction (parallel to the X–Y plane). The selected source positions of the rays are situated in the inner region of the plasma torus, as indicated by the blue launch points in Panels (b) and (d). Consequently, the horizontally launched rays in Panels (e)–(f) are directed toward the plasma torus, and they are quickly reflected at the boundary of the plasma torus, resulting in vertical propagation (toward the z-axis direction in Panels (e)–(f)).

The calculation results for the Z mode emissions are presented in Figure 9. Panels (a)–(b) show the results for the 5 kHz band, which are comparable to the outcomes in Figure 6 Panels (a)–(c). The 5 kHz Z mode rays propagate and fill the TR and are primarily reflected at the f_z surface. Similarly, Panels (c)–(d) display the raypaths for the 20 kHz Z mode emissions, but with source regions shifted inward if compared to Figures 6 and 7, deviating from the CMI and UHW predicted positions. Some intriguing rays are observed to cross the equator in the region between the planet and the plasma torus in Panels (d), either when propagating toward these areas or being reflected at the inner edge of the plasma torus or the ionosphere. However, the electron density model does not consider the possible presence of the ring ionosphere in this region, which may hinder direct propagation of Z mode emissions, as discussed in Section 8. In Panels (e)–(f) of Figure 9, the Z mode rays are launched horizontally at both 5 and 20 kHz bands. Some 5 kHz Z mode emissions launched at positions with smaller z-axis values can be reflected at the f_z surface and they are reflected vertically near the plasma torus boundary. These rays then

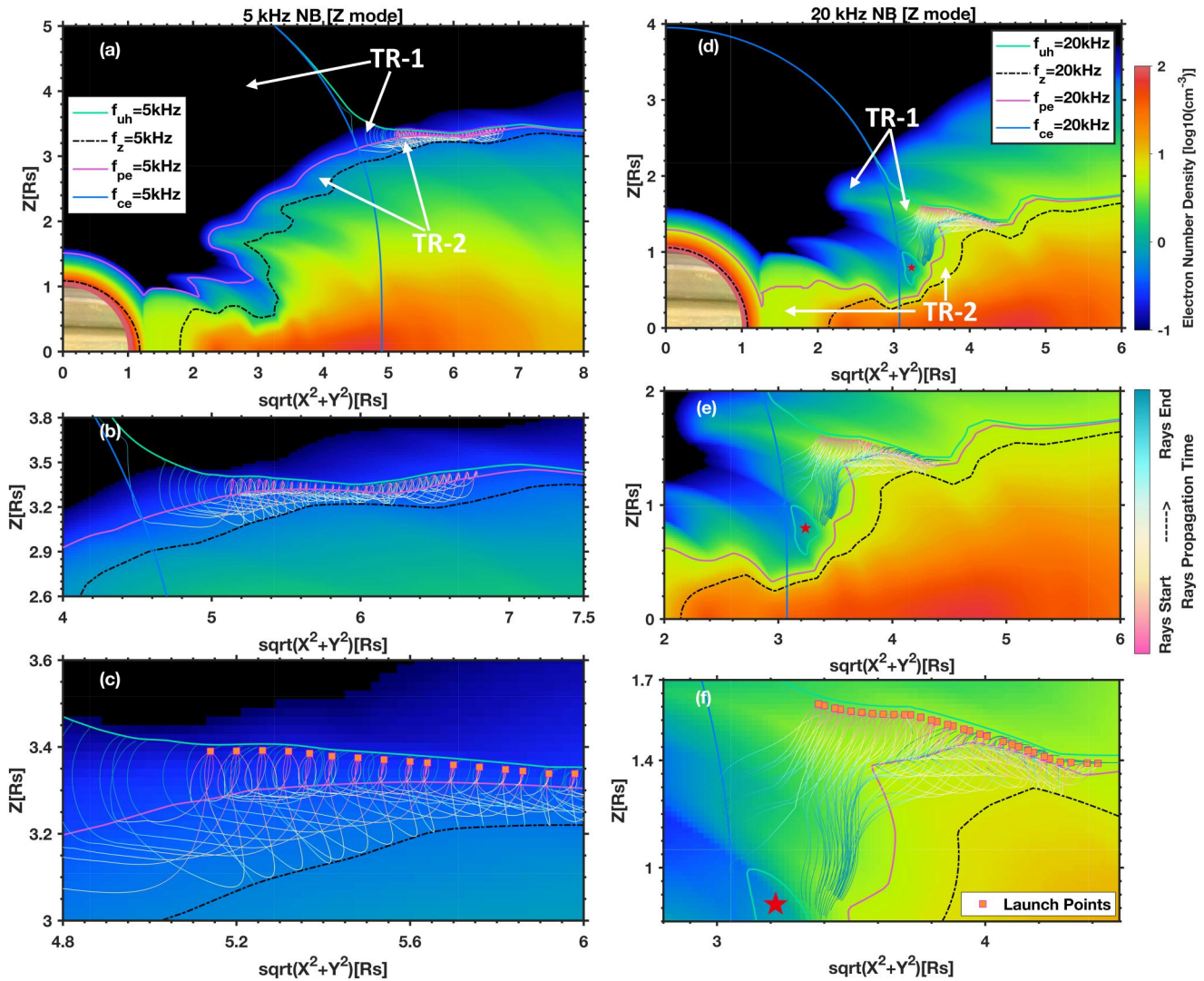


Figure 7. Z mode Narrowband propagation within the Saturnian magnetosphere using the UHW source parameters. Panels (a)–(c) and Panels (d)–(f) display the ray-tracing calculation results for 5 and 20 kHz Z mode emissions, respectively, using the UHW source parameters, following the same format as Figure 6.

propagate straight until they encounter the f_{uh} surface, where they get into resonance and stop as shown in Panel (e). In contrast, other rays launched at positions with larger z -axis values directly reach the f_{uh} surface and stop. This trend is more evident in Panel (f) for 20 kHz Z mode waves, as the TR for 20 kHz is smaller. The calculation results in Figures 8 and 9 may be applicable to NB emissions' propagation scenarios when the magnetosphere is highly perturbed, and the plasma torus deviates from its average state.

8. Discussion and Summary

This study investigates the propagation characteristics of Saturn NB emissions using a 3-D ray-tracing method. A new Saturn's electron density model has been derived based on several existing models (Persoon et al., 2006, 2019, 2020), which provides the electron density information from Saturn's ionosphere to the plasma torus. The global propagation patterns of both the L-O mode and Z mode emissions at both 5 and 20 kHz frequency bands are derived.

The ray-tracing calculations for the 5 kHz Z mode NB emissions, utilizing the CMI theory predicted source region and initial WNA, provide a closer alignment with observations, showing that the 5 kHz Z mode rays can fill the inner region close to Saturn (TR-1, TR-2) and reproduce the observed wave distribution map from Wu

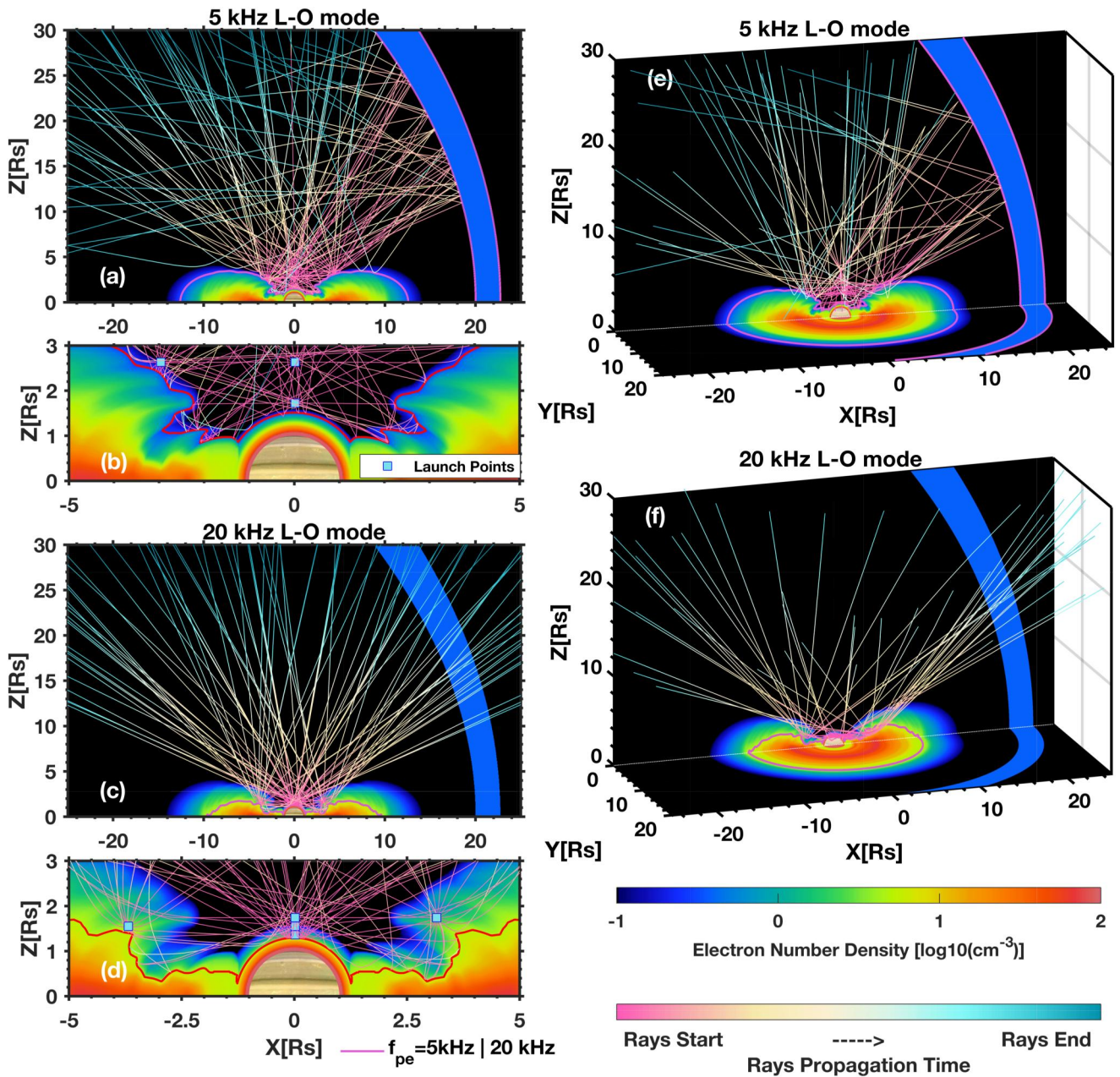


Figure 8. L-O mode emissions propagation within the Saturnian magnetosphere. Panel (a) displays the propagation paths of the 5 kHz L-O emissions in the meridional plane, with the initial propagation angles restricted to the meridional plane. Panel (b) provides a zoom-in view of Panel (a), specifically near Saturn. Panels (c)–(d) present similar results for the 20 kHz L-O mode emissions in the same format as Panels (a)–(b). Panels (e)–(f) illustrate the raypaths in a 3D view for both the 5 and 20 kHz L-O mode emissions, with the rays launched in different directions within a horizontal plane. For clarity, only two slices in the X–Y and X–Z planes of the background density are shown. The color-code corresponds to the background electron density, while the pink contour lines delineate the regions where f_{pe} equals 5 and 20 kHz, respectively.

et al. (2021). The ray-tracing calculations reveal potential trapping of Z mode emissions near the slot region at the north-south boundary of the plasma torus. This TR is formed by the local minimum of the plasma density, as equivalently the local minimum of the low-frequency cut-off of f_z surfaces. Such trapping processes may contribute to the enhancement of emissions and the possible depolarization of the emissions. However, in this study, we did not consider the auroral sources or even the ionospheric sources of the 5 kHz Z mode NB emissions, as reported in previous studies (Menietti et al., 2015, 2018b; Ye et al., 2009). Identifying these sources is challenging since the CMI parameters used in our model do not identify possible auroral sources due to the limit

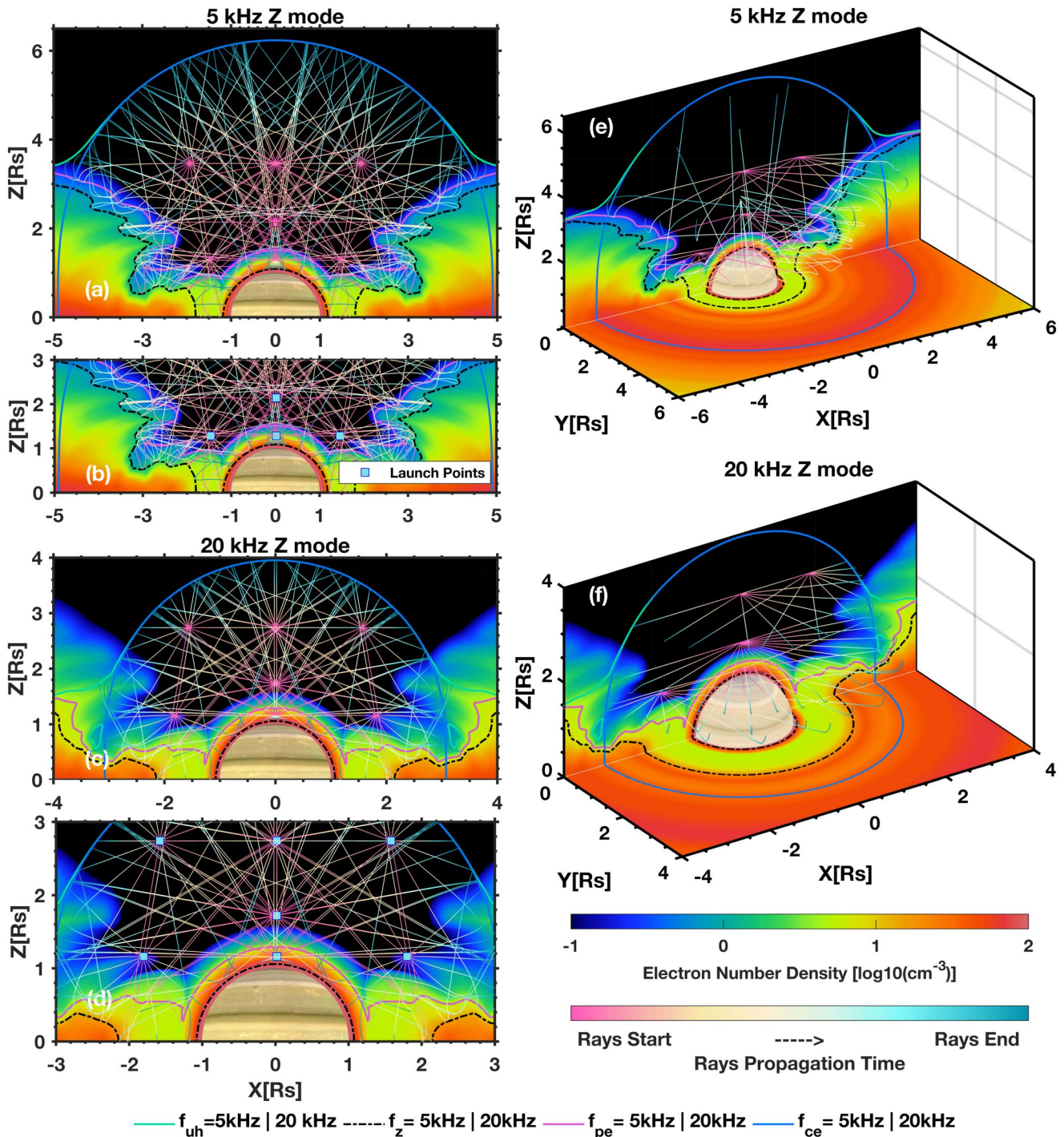


Figure 9. Z mode emissions propagation within the Saturnian magnetosphere. Panels (a)–(d) provide the propagation paths of the 5 and 20 kHz Z mode emissions in the meridional plane, with the initial propagation angles restricted to the meridional plane, following the same format as Figure 8 Panels (a)–(d). Panels (e)–(f) illustrate the Z mode emissions propagation paths in a 3D view for both the 5 and 20 kHz bands, with the rays launched in different directions within a horizontal plane, also in the same format as Figure 8 Panels (e)–(f). The green, black dashed, pink, and blue contour lines delineate the regions where f_{uh} , f_z , f_{pe} , and f_{ce} equal 5 and 20 kHz, respectively.

of the f_{pe}/f_{ce} ratio demand ($0.28 \sim 1$ used for the 5 kHz Z mode waves as described in Table 2). If these sources exist, these potential auroral sources will lie in a region with $f_{pe}/f_{ce} < 0.3$ or even < 0.1 , which contradicts the calculations of Melrose et al. (1984) due to the demanded limits of 0.3–1 for the f_{pe}/f_{ce} ratio, as outlined for the

5 kHz Z mode waves in Table 2. Although the direction-finding analysis suggests possible source regions near the SKR source region, there are currently no further observations that support this. A calculation of the growth rate in the vicinity of an SKR source region suggests that the observed Z mode and O mode emissions may come from another direction (Menietti et al., 2011). According to the ray-tracing results in this work, there is a possibility that the observed auroral origin Z mode emissions may come from the reflection of the Z mode waves in the ionosphere. If the auroral sources of the Z mode NB emissions truly exist, the propagation pattern of these waves should be similar to the results as illustrated in Figure 9, as the arbitrarily chosen sources launched toward all the 2π directions could account for the possible auroral sources.

The ray-tracing calculations for the 5 kHz Z mode NB emissions, utilizing the UHW theory predicted source region and initial WNA, suggest that these rays are limited to the north-south edges of the plasma torus and essentially trapped between f_z and f_{uh} surfaces (as shown in Figure 7). They can not contribute to the 5 kHz Z mode observed closer to Saturn as reported in Wu et al. (2021); however, these sources should not be ruled out because they can also significantly contribute to the 5 kHz L-O mode emissions observed in this region (after mode conversion), although no 5 kHz Z mode emission is indeed observed in these predicted regions so far.

The ray-tracing calculations of the 20 kHz Z mode rays, predicted by the CMI theory to originate from the north-south edges of the plasma torus, tend to be confined by the plasma parameters in our model. These emissions cannot escape from the source regions and propagate very far before facing their resonance again. An important factor preventing the propagation of 20 kHz Z mode waves toward Saturn is their resonance frequency, which is close to the local f_{ce} surfaces, hence most simulated rays are outside of the $f_{ce} = 20$ kHz contour (as shown in Figures 6 and 7). The simulations of 20 kHz Z mode waves using the UHW theory provide similar pictures as for the CMI sources. This propagation feature appears somewhat contradictory to the fact that 20 kHz Z mode emissions are also observed across a large portion of the TR (Menietti, Averkamp, Ye, Persoon, et al., 2018; Wu et al., 2021). Merely placing new 20 kHz Z-mode sources closer to Saturn could potentially replicate the observed characteristics, as shown in Figure 9. However, these source regions would contradict the growth rate calculations proposed by Melrose et al. (1984), which necessitate a plasma condition in the radio source region with a ratio of $0.3 < f_{pe}/f_{ce} < 1.3$. The observed 20 kHz Z mode emissions in the TR may then simply imply that the plasma torus configuration is highly dynamic, letting the 20 kHz Z mode waves escape from the source region.

The ray-tracing calculations for both the 5 kHz & 20 kHz L-O mode NB emissions, by assuming the L-O mode waves are mode converted from the Z mode waves along the f_{pe} surfaces, provide consistent propagation pictures as derived from data observation in Wu et al. (2021). The L-O mode emissions preferentially propagate to higher latitudes due to the hindrance of the plasma torus. These rays can cross the polar region from one side of the planet to the other side and possibly have an azimuthal component, as shown in Figure 8. Notably, the L-O mode NB emissions, particularly at 5 kHz, can undergo multiple reflections within the slot region that formed by the local minimum of the low-frequency cut-off at f_{pe} surfaces, potentially resulting in wave trapping and depolarization.

The previous work of Ye, Gurnett, et al. (2010) predicted that the Z mode NB emissions may cross the equator, which is explained as potential candidates for causing the dual rotation periods in NB emissions. However, neither 5 kHz nor 20 kHz Z mode rays from CMI/UHW sources are able to cross the equator, as illustrated in Figures 6 and 7, except for time periods under highly dynamical magnetospheric conditions, as suggested by Figure 9. One factor not considered in our simulation is the ring ionosphere of Saturn located in this equatorial region inside the inner edge of the plasma torus (Luhmann et al., 2006), which may increase the electron density and inhibit Z mode waves from crossing the equator. However, whether there are “gaps” between the rings and the plasma torus is still unknown, which may allow the Z mode waves to cross. There are several possible mechanisms for the generation of the dual modulation periods in NB emissions, for example, (a) the Z mode waves are indeed able to cross the equator; (b) Z mode waves mode convert to whistler mode emissions and cross the equator; (c) the reflection of the 5 kHz L-O mode NB emissions to the other hemisphere by the magnetosheath (this only applies to 5 kHz band); (d) two modulation periods are intrinsic to the CMI-unstable energetic electrons bouncing between both hemispheres, as proposed by Kivelson and Jia (2018). Further studies regarding this feature are required and it is therefore left here.

The whistler mode NB emission at 5 kHz was reported only once by Menietti, Averkamp, Ye, Sulaiman, et al. (2018) in the equatorial ionosphere of Saturn during Cassini's last year orbit. These whistler mode NB emissions usually have to propagate under conditions where $f_{pe}/f_{ce} < 1$ as shown by Figure 4 Panels (c) and (f). The

source of these whistler mode NB emissions could be a mode conversion from the Z mode waves at the f_{pe} surfaces. Once the whistler mode NB emissions leave the source region, they should mostly propagate field-aligned with smaller WNA within the propagation zones, as illustrated by Figure 4 Panels (c) and (f).

To summarize, the L-O mode NB emissions, generated along the local f_{pe} surfaces through mode conversion from Z mode waves, exhibit straight-line propagation but are subject to reflections between the ionosphere, the plasma torus, and the magnetosheath (the later only applies to the 5 kHz band). The slot region, characterized by lower electron density and distributed around the plasma torus boundary, significantly influences the propagation of NB emissions and can lead to trapping and depolarization of emissions. The 5 kHz Z mode NB emissions can propagate and fill the TR. In contrast, the 20 kHz Z mode NB emissions are predominantly trapped near the source regions located at the north-south edges of the plasma torus and possibly escape the source region when the plasma environment is appropriate. These propagation features of Saturn NB emissions may provide implications for the propagation characteristics of the other radio components at the other planets, such as the narrow-band Kilometric emission (n-KOM; Reiner et al., 1993) at Jupiter.

Data Availability Statement

The Cassini RPWS data used in this work were downloaded from the LESIA/Kronos collection of n2 level (Cecconi et al., 2017a) and n3e level (Cecconi et al., 2017b) (goniopolarimetric inversion results obtained following the method of Cecconi & Zarka., 2005). The Artemis-P source code can be found at Gautier et al. (2023). The electron density profile derived in Section 2 and adapted to the ray-tracing calculations is also available at Wu, U, et al. (2023).

References

- Appleton, E. V. (1928). The influence of the earth's magnetic field on wireless transmission (summary). In *U.R.S.I. Proc.* 1927.
- Appleton, E. V. (1932). Wireless studies of the ionosphere. *Journal of the Institution of Electrical Engineers*, 71(21), 257–265. <https://doi.org/10.1049/pws.1932.0027>
- Beghin, C., Rauch, J. L., & Bosqued, J. M. (1989). Electrostatic plasma waves and HF auroral hiss generated at low altitude. *Journal of Geophysical Research*, 94(A2), 1359–1378. <https://doi.org/10.1029/JA094iA02p01359>
- Benson, R. F., Webb, P. A., Green, J. L., Carpenter, D. L., Sonwalkar, V. S., James, H. G., & Reinisch, B. W. (2006). Active wave experiments in space plasmas: The Z mode. In J. W. LaBelle & R. A. Treumann (Eds.), *Geospace electromagnetic waves and radiation* (pp. 3–35). Springer Berlin Heidelberg. https://doi.org/10.1007/3-540-33203-0_1
- Burkholder, B. L., Delamere, P. A., Johnson, J. R., & Ng, C.-S. (2020). Identifying active Kelvin–Helmholtz vortices on Saturn's magnetopause boundary. *Geophysical Research Letters*, 47(1), e2019GL084206. <https://doi.org/10.1029/2019GL084206>
- Cecconi, B., Lamy, L., & Zarka, P. (2017a). Cassini/RPWS/HFR LESIA/Kronos N2 data collection (version 1.0) [Dataset]. *PADC*. <https://doi.org/10.25935/XS9J-ND90>
- Cecconi, B., Lamy, L., & Zarka, P. (2017b). Cassini/RPWS/HFR LESIA/Kronos N3e Data Collection (Version 1.0) [Dataset]. *PADC*. <https://doi.org/10.25935/9ZAB-FP47>
- Cecconi, B., & Zarka, P. (2005). Direction finding and antenna calibration through analytical inversion of radio measurements performed using a system of two or three electric dipole antennas on a three-axis stabilized spacecraft. *Radio Science*, 40(3), 1–20. <https://doi.org/10.1029/2004RS003070>
- Crema, S., Llena, M., Calsamiglia, A., Estrany, J., Marchi, L., Vericat, D., & Cavalli, M. (2020). Can inpainting improve digital terrain analysis? Comparing techniques for void filling, surface reconstruction and geomorphometric analyses. *Earth Surface Processes and Landforms*, 755(January), 736–755. <https://doi.org/10.1002/esp.4739>
- Dougherty, M. K., Cao, H., Khurana, K. K., Hunt, G. J., Provan, G., Kellock, S., et al. (2018). Saturn's magnetic field revealed by the Cassini Grand Finale. *Science*, 362(6410). <https://doi.org/10.1126/science.aat5434>
- Echer, E. (2019). Solar wind and interplanetary shock parameters near Saturn's orbit (~10 AU). *Planetary and Space Science*, 165, 210–220. <https://doi.org/10.1016/j.pss.2018.10.006>
- Ellis, G. R. (1956). The z propagation hole in the ionosphere. *Journal of Atmospheric and Terrestrial Physics*, 8(1), 43–54. [https://doi.org/10.1016/0021-9169\(56\)90090-3](https://doi.org/10.1016/0021-9169(56)90090-3)
- Fischer, G., Gurnett, D. A., Kurth, W. S., Ye, S.-Y., & Groene, J. B. (2015). Saturn kilometric radiation periodicity after equinox. *Icarus*, 254, 72–91. <https://doi.org/10.1016/j.icarus.2015.03.014>
- Gautier, A.-L. (2013). *Étude de la propagation des ondes radio dans les environnements planétaires* (Doctoral dissertation). Observatoire de Paris. Retrieved from <https://theses.hal.science/tel-01145651v2>
- Gautier, A. L., Baskevitch, C. A., & Cecconi, B. (2023). *maserlib/ARTEMIS-P: Version 0.1.0 (v0.1.0)*. Zenodo. <https://doi.org/10.5281/zenodo.8055943>
- Gautier, A.-L., Cecconi, B., & Zarka, P. (2013). ARTEMIS-P: A general Ray Tracing code in anisotropic plasma for radioastronomical applications. In *Proceedings of the 2013 international symposium on electromagnetic theory* (pp. 1–4).
- Gurnett, D. A. (1998). Principles of space plasma wave instrument design. In *Measurement techniques in space plasmas* (pp. 121–136). American Geophysical Union (AGU). <https://doi.org/10.1002/9781118664391.ch14>
- Gurnett, D. A. (2020). The origins of space radio and plasma wave research at the University of Iowa. *Journal of Geophysical Research: Space Physics*, 125(2), 1–16. <https://doi.org/10.1029/2019ja027324>
- Gurnett, D. A., Kurth, W. S., Kirchner, D. L., Hospodarsky, G. B., Averkamp, T. F., Zarka, P., et al. (2004). The Cassini radio and plasma wave investigation. *Space Science Reviews*, 114(1), 395–463. <https://doi.org/10.1007/s11214-004-1434-0>

Acknowledgments

This work was supported by the Strategic Priority Research Program of the Chinese Academy of Sciences (Grant XDB 41000000). SY and SW thank the support of NSFC projects 42274221 and 42074180. We thank the support of Science, Technology and Innovation Commission of Shenzhen Municipality program (STIC20200925153725002). SY and SW thank the support of the Guangdong province program (Grant 2021CX02Z468). UT and GF acknowledge support from the FWF-GACR international project I4559-N/20-06802L. C.M.J.'s work was supported by the Science Foundation Ireland Grant 18/FRL/6199.

- Gurnett, D. A., Kurth, W. S., & Scarf, F. L. (1981). Narrowband electromagnetic emissions from Saturn's magnetosphere. *Nature*, 292(5825), 733–737. <https://doi.org/10.1038/292733a0>
- Gurnett, D. A., Persoon, A. M., Groene, J. B., Kopf, A. J., Hospodarsky, G. B., & Kurth, W. S. (2009). A north-south difference in the rotation rate of auroral hiss at Saturn: Comparison to Saturn's kilometric radio emission. *Geophysical Research Letters*, 36(21). <https://doi.org/10.1029/2009GL040774>
- Hartree, D. R. (1931). The propagation of electromagnetic waves in a refracting medium in a magnetic field. *Mathematical Proceedings of the Cambridge Philosophical Society*, 27(1), 143–162. <https://doi.org/10.1017/s0305004100009440>
- Haselgrove, C. B., & Haselgrove, J. (1960). Twisted ray paths in the ionosphere. *Proceedings of the Physical Society*, 75(3), 357–363. <https://doi.org/10.1088/0370-1328/75/3/304>
- Haselgrove, J. (1963). The Hamiltonian ray path equations. *Journal of Atmospheric and Terrestrial Physics*, 25(7), 397–399. [https://doi.org/10.1016/0021-9169\(63\)90173-9](https://doi.org/10.1016/0021-9169(63)90173-9)
- Jackman, C. M., & Arridge, C. S. (2011). Solar cycle effects on the dynamics of Jupiter's and Saturn's magnetospheres. *Solar Physics*, 274(1), 481–502. <https://doi.org/10.1007/s11207-011-9748-z>
- Jackman, C. M., Thomsen, M. F., & Dougherty, M. K. (2019). Survey of Saturn's magnetopause and bow shock positions over the entire Cassini Mission: Boundary statistical properties and exploration of associated upstream conditions. *Journal of Geophysical Research: Space Physics*, 124(11), 8865–8883. <https://doi.org/10.1029/2019JA026628>
- Kanani, S. J., Arridge, C. S., Jones, G. H., Fazakerley, A. N., McAndrews, H. J., Sergis, N., et al. (2010). A new form of Saturn's magnetopause using a dynamic pressure balance model, based on in situ, multi-instrument Cassini measurements. *Journal of Geophysical Research*, 115(A6), A06207. <https://doi.org/10.1029/2009JA014262>
- Kinrade, J., Badman, S. V., Paranicas, C., Jackman, C. M., Louis, C. K., & O'Dwyer, E. P. (2023). Testing the relationship between Saturn's ENA and narrowband radio emissions. In C. K. Louis, C. M. Jackman, G. Fischer, A. H. Sulaiman, P. Zucca, & D. Institute for Advanced Studies (Eds.), *Planetary, solar and heliospheric radio emissions IX*. <https://doi.org/10.25546/103101>
- Kivelson, M. G., & Jia, X. (2018). Coupled SKR emissions in Saturn's northern and southern ionospheres. *Geophysical Research Letters*, 45(7), 2893–2900. <https://doi.org/10.1002/2017GL075425>
- Kurth, W. S., Ashour-Abdalla, M., Frank, L. A., Kennel, C. F., Gurnett, D. A., Sentman, D. D., & Burek, B. G. (1979). A comparison of intense electrostatic waves near f_{UHR} with linear instability theory. *Geophysical Research Letters*, 6(6), 487–490. <https://doi.org/10.1029/GL006i006p00487>
- Kurth, W. S., Craven, J. D., Frank, L. A., & Gurnett, D. A. (1979). Intense electrostatic waves near the upper hybrid resonance frequency. *Journal of Geophysical Research*, 84(A8), 4145–4164. <https://doi.org/10.1029/JA084iA08p04145>
- Lamy, L. (2011). Variability of southern and northern SKR periodicities. In H. O. Rucker, W. S. Kurth, P. Louarn, & G. Fischer (Eds.), *Planetary radio emissions VII* (pp. 39–50). Verlag der Österreichischen Akademie der Wissenschaften. <https://doi.org/10.1553/PRE7s39>
- Lamy, L., Cecconi, B., Prangé, R., Zarka, P., Nichols, J. D., & Clarke, J. T. (2009). An auroral oval at the footprint of Saturn's kilometric radio sources, collocated with the UV aurorae. *Journal of Geophysical Research*, 114(A10). <https://doi.org/10.1029/2009JA014401>
- Luhmann, J. G., Johnson, R. E., Tokar, R. L., Ledvina, S. A., & Cravens, T. E. (2006). A model of the ionosphere of Saturn's rings and its implications. *Icarus*, 181(2), 465–474. <https://doi.org/10.1016/j.icarus.2005.11.022>
- Ma, X., Delamere, P. A., Schok, A., Wing, S., Johnson, J. R., & Liou, Y.-L. (2022). Jupiter's sheared flow unstable magnetopause boundary observed by Juno. *Journal of Geophysical Research: Space Physics*, 127(10), e2022JA030719. <https://doi.org/10.1029/2022JA030719>
- McIlwain, C. E. (1966). Magnetic coordinates. *Space Science Reviews*, 5(5), 585–598. <https://doi.org/10.1007/BF00167327>
- Melrose, D. B., Hewitt, R. G., & Dulk, G. A. (1984). Electron-cyclotron maser emission: Relative growth and damping rates for different modes and harmonics. *Journal of Geophysical Research*, 89(A2), 897–904. <https://doi.org/10.1029/JA089iA02p00897>
- Menietti, J. D., Averkamp, T. F., Ye, S.-Y., Horne, R. B., Woodfield, E. E., Shprits, Y. Y., et al. (2015). Survey of Saturn Z-mode emission. *Journal of Geophysical Research: Space Physics*, 120(8), 6176–6187. <https://doi.org/10.1002/2015JA021426>
- Menietti, J. D., Averkamp, T. F., Ye, S.-Y., Persoon, A. M., Morooka, M. W., Groene, J. B., & Kurth, W. S. (2018). Extended survey of Saturn Z-Mode wave intensity through Cassini's final orbits. *Geophysical Research Letters*, 45(15), 7330–7336. <https://doi.org/10.1029/2018GL079287>
- Menietti, J. D., Averkamp, T. F., Ye, S.-Y., Sulaiman, A. H., Morooka, M. W., Persoon, A. M., et al. (2018). Analysis of intense Z-Mode emission observed during the Cassini Proximal orbits. *Geophysical Research Letters*, 45(14), 6766–6772. <https://doi.org/10.1002/2018GL077354>
- Menietti, J. D., Mutel, R. L., Schippers, P., Ye, S.-Y., Gurnett, D. A., & Lamy, L. (2011). Analysis of Saturn kilometric radiation near a source center. *Journal of Geophysical Research*, 116(A12), A12222. <https://doi.org/10.1029/2011JA017056>
- Menietti, J. D., Ye, S.-Y., Yoon, P. H., Santolík, O., Rymer, A. M., Gurnett, D. A., & Coates, A. J. (2009). Analysis of narrowband emission observed in the Saturn magnetosphere. *Journal of Geophysical Research*, 114(A6), A06206. <https://doi.org/10.1029/2008JA013982>
- Menietti, J. D., Yoon, P. H., Pisa, D., Averkamp, T. F., Sulaiman, A. H., Kurth, W. S., et al. (2019). The role of intense upper hybrid resonance emissions in the generation of Saturn narrowband emission. *Journal of Geophysical Research: Space Physics*, 124(7), 5709–5718. <https://doi.org/10.1029/2019JA026855>
- Menietti, J. D., Yoon, P. H., Pisa, D., Ye, S.-Y., Santolík, O., Arridge, C. S., et al. (2016). Source region and growth analysis of narrowband Z-mode emission at Saturn. *Journal of Geophysical Research: Space Physics*, 121(12), 11911–929942. <https://doi.org/10.1002/2016JA022913>
- Menietti, J. D., Yoon, P. H., Ye, S. Y., Cecconi, B., & Rymer, A. M. (2010). Source mechanism of Saturn narrowband emission. *Annales Geophysicae*, 28(4), 1013–1021. <https://doi.org/10.5194/angeo-28-1013-2010>
- Mitchell, D. G., Brandt, P. C., Carbary, J. F., Kurth, W. S., Krimigis, S. M., Paranicas, C., et al. (2015). Injection, interchange, and reconnection. In *Magnetotails in the solar system* (pp. 327–343). American Geophysical Union (AGU). <https://doi.org/10.1002/9781118842324.ch19>
- Persoon, A. M., Gurnett, D. A., Kurth, W. S., & Groene, J. B. (2006). A simple scale height model of the electron density in Saturn's plasma disk. *Geophysical Research Letters*, 33(18). <https://doi.org/10.1029/2006GL027090>
- Persoon, A. M., Kurth, W. S., Gurnett, D. A., Faden, J. B., Groene, J. B., Morooka, M. W., et al. (2020). Distribution in Saturn's inner magnetosphere from 2.4 to 10 RS: A diffusive equilibrium model. *Journal of Geophysical Research: Space Physics*, 125(3), 1–15. <https://doi.org/10.1029/2019JA027545>
- Persoon, A. M., Kurth, W. S., Gurnett, D. A., Groene, J. B., Sulaiman, A. H., Wahlund, J. E., et al. (2019). Electron density distributions in Saturn's ionosphere. *Geophysical Research Letters*, 46(6), 3061–3068. <https://doi.org/10.1029/2018GL078020>
- Reiner, M. J., Fainberg, J., Stone, R. G., Kaiser, M. L., Desch, M. D., Manning, R., et al. (1993). Source characteristics of Jovian narrow-band kilometric radio emissions. *Journal of Geophysical Research*, 98(E7), 13163–13176. <https://doi.org/10.1029/93JE00536>
- Stix, T. H. (1992). *Waves in plasmas*. Springer Science & Business Media.
- Wang, Z., Gurnett, D. A., Fischer, G., Ye, S.-Y., Kurth, W. S., Mitchell, D. G., et al. (2010). Cassini observations of narrowband radio emissions in Saturn's magnetosphere. *Journal of Geophysical Research*, 115(A6), A06213. <https://doi.org/10.1029/2009JA014847>

- Went, D. R., Hospodarsky, G. B., Masters, A., Hansen, K. C., & Dougherty, M. K. (2011). A new semiempirical model of Saturn's bow shock based on propagated solar wind parameters. *Journal of Geophysical Research*, *116*(A7), A07202. <https://doi.org/10.1029/2010JA016349>
- Wing, S., Brandt, P. C., Mitchell, D. G., Johnson, J. R., Kurth, W. S., & Menietti, J. D. (2020). Periodic narrowband radio wave emissions and inward plasma transport at Saturn's magnetosphere. *The Astronomical Journal*, *159*(6), 249. <https://doi.org/10.3847/1538-3881/ab818d>
- Woodfield, E. E., Horne, R. B., Glauert, S. A., Menietti, J. D., Shprits, Y. Y., & Kurth, W. S. (2018). Formation of electron radiation belts at Saturn by Z-mode wave acceleration. *Nature Communications*, *9*(1), 5–11. <https://doi.org/10.1038/s41467-018-07549-4>
- Wu, C. S., & Lee, L. C. (1979). A theory of the terrestrial kilometric radiation. *The Astrophysical Journal*, *230*(July), 621. <https://doi.org/10.1086/157120>
- Wu, S. Y., Ye, S. Y., Fischer, G., Jackman, C. M., Wang, J., Menietti, J. D., et al. (2022). Reflection and refraction of the L-O Mode 5 kHz Saturn narrowband emission by the magnetosheath. *Geophysical Research Letters*, *49*(5), e2021GL096990. <https://doi.org/10.1029/2021GL096990>
- Wu, S. Y., Ye, S. Y., Fischer, G., Wang, J., Kurth, W. S., Yao, Z. H., et al. (2023). Phase locking among Saturn radio emissions revealed by Cassini observations. *A&A*, *680*, A7. <https://doi.org/10.1051/0004-6361/202347279>
- Wu, S. Y., Ye, S. Y., Fischer, G., Wang, J., Long, M., Menietti, J. D., et al. (2021). Statistical study on spatial distribution and polarization of Saturn narrowband emissions. *The Astrophysical Journal*, *918*(2), 64. <https://doi.org/10.3847/1538-4357/ac0af1>
- Wu, S. Y., U. T., Ye, S. Y., Fischer, G., Cecconi, B., Wang, M. M., et al. (2023). Saturn electron model derived from “Raytracing analysis for the propagation of Saturn narrowband emission within the Saturnian magnetosphere” (Version 1.0) [Dataset]. *PADC*. <https://doi.org/10.25935/4fm1-xh69>
- Ye, S.-Y., Fischer, G., Kurth, W. S., Menietti, J. D., & Gurnett, D. A. (2016). Rotational modulation of Saturn's radio emissions after equinox. *Journal of Geophysical Research: Space Physics*, *121*(12), 11711–11747. <https://doi.org/10.1002/2016JA023281>
- Ye, S.-Y., Gurnett, D. A., Fischer, G., Cecconi, B., Menietti, J. D., Kurth, W. S., et al. (2009). Source locations of narrowband radio emissions detected at Saturn. *Journal of Geophysical Research*, *114*(A6), A06219. <https://doi.org/10.1029/2008JA013855>
- Ye, S.-Y., Gurnett, D. A., Groene, J. B., Wang, Z., & Kurth, W. S. (2010). Dual periodicities in the rotational modulation of Saturn narrowband emissions. *Journal of Geophysical Research*, *115*(A12), A12258. <https://doi.org/10.1029/2010JA015780>
- Ye, S.-Y., Menietti, J. D., Fischer, G., Wang, Z., Cecconi, B., Gurnett, D. A., & Kurth, W. S. (2010). Z mode waves as the source of Saturn narrowband radio emissions. *Journal of Geophysical Research*, *115*(A8), A08228. <https://doi.org/10.1029/2009JA015167>
- Yi, S., Lee, S., Kim, H., Lim, D., Seough, J., Yoon, P. H., et al. (2013). Z -mode maser instability. *Journal of Geophysical Research: Space Physics*, *118*(October), 7584–7592. <https://doi.org/10.1002/2013JA019376>
- Yoon, P. H., Weatherwax, A. T., Rosenberg, T. J., & LaBelle, J. (1996). Lower ionospheric cyclotron maser theory: A possible source of 2fce and 3fce auroral radio emissions. *Journal of Geophysical Research*, *101*(A12), 27015–27025. <https://doi.org/10.1029/96ja02664>
- Yoon, P. H., Weatherwax, A. T., Rosenberg, T. J., LaBelle, J., & Shepherd, S. G. (1998). Propagation of medium frequency (1–4 MHz) auroral radio waves to the ground via the Z-mode radio window. *Journal of Geophysical Research*, *103*(A12), 29267–29275. <https://doi.org/10.1029/1998ja900032>